Title

Noise Characterization and Filtering in the MicroBooNE Liquid Argon TPC

Journal

Journal of Instrumentation, 12(08)

ISSN

1748-0221

Authors

Acciarri, R
Adams, C
An, R
et al.

Publication Date

2017-08-01

DOI

10.1088/1748-0221/12/08/p08003

Peer reviewed

Prepared for submission to JINST

Noise Characterization and Filtering in the MicroBooNE Liquid Argon TPC

The MicroBooNE Collaboration

R. Acciarri[g] C. Adams[bb,1] R. An[h] J. Anthony[c] J. Asaadi[y] M. Auger[a] L. Bagby[g] S. Balasubramanian[bb] B. Baller[g] C. Barnes[n] G. Barr[q] M. Bass[q] F. Bay[z] M. Bishai[b] A. Blake[j] T. Bolton[i] B. Bullard[b] L. Camilleri[f] D. Caratelli[f] B. Carls[g] R. Castillo Fernandez[g] F. Cavanna[g] H. Chen[b] E. Church[r] D. Cianci[l,f] E. Cohen[w] G. H. Collin[m] J. M. Conrad[m] M. Convery[u] J. I. Crespo-Anadón[f] G. De Geronimo[b] M. Del Tutto[q] D. Devitt[j] S. Dytman[s] B. Eberly[u] A. Ereditato[a] L. Escudero Sanchez[c] J. Esquivel[v] A. A. Fadeeva[f] B. T. Fleming[bb] W. Foreman[d] A. P. Furmanski[l] D. Garcia-Gamez[l] G. T. Garvey[k] V. Genty[f] D. Goeldi[a] S. Gollapinni[i,x] N. Graf[s] E. Gramellini[bb] H. Greenlee[g] R. Grosso[e] R. Guenette[q] A. Hackenburg[bb] P. Hamilton[v] O. Hen[m] J. Hewes[l] C. Hill[l] J. Ho[d] G. Horton-Smith[i] A. Hourlier[m] E.-C. Huang[k] C. James[g] J. Jan de Vries[c] C.-M. Jen[aa] L. Jiang[s] R. A. Johnson[e] J. Joshi[b] H. Jostlein[g] D. Kaleko[f] G. Karagiorgi[l,f] W. Ketchum[g] B. Kirby[b] M. Kirby[g] T. Kobilarcik[g] I. Kreslo[a] A. Laube[q] S. Li[b] Y. Li[b] A. Lister[j] B. R. Littlejohn[h] S. Lockwitz[g] D. Lorca[a] W. C. Louis[k] M. Luethi[a] B. Lundberg[g] X. Luo[bb] A. Marchionni[g] C. Mariani[aa] J. Marshall[c] D. A. Martinez Caicedo[h] V. Meddage[i] T. Miceli[o] G. B. Mills[k] J. Moon[m] M. Mooney[b] C. D. Moore[g] J. Mousseau[n] R. Murrells[l] D. Naples[s] P. Nienaber[t] J. Nowak[j] O. Palamara[g] V. Paolone[s] V. Papavassiliou[o] S. F. Pate[o] Z. Pavlovic[g] E. Piasetzky[w] D. Porzio[l] G. Pulliam[v] X. Qian[b] J. L. Raaf[g] V. Radeka[b] A. Rafique[i] S. Rescia[b] L. Rochester[u] C. Rudolf von Rohr[a] B. Russell[bb] D. W. Schmitz[d] A. Schukraft[g] W. Seligman[f] M. H. Shaevitz[f] J. Sinclair[a] A. Smith[c] E. L. Snider[g] M. Soderberg[v] S. Söldner-Rembold[l] S. R. Soleti[q] P. Spentzouris[g] J. Spitz[n] J. St. John[e] T. Strauss[g] A. M. Szelc[l] N. Tagg[p] K. Terao[f] M. Thomson[c] C. Thorn[b] M. Toups[g] Y.-T. Tsai[u] S. Tufanli[bb] T. Usher[u] W. Van De Pontseele[q] R. G. Van de Water[k] B. Viren[b] M. Weber[a] D. A. Wickremasinghe[s] S. Wolbers[g] T. Wongjirad[m] K. Woodruff[o] T. Yang[g] L. Yates[m] B. Yu[b] G. P. Zeller[g] J. Zennamo[d] C. Zhang[b]

[a] *Universität Bern, Bern CH-3012, Switzerland*

[b] *Brookhaven National Laboratory (BNL), Upton, NY, 11973, USA*

[c] *University of Cambridge, Cambridge CB3 0HE, United Kingdom*

[d] *University of Chicago, Chicago, IL, 60637, USA*

[e] *University of Cincinnati, Cincinnati, OH, 45221, USA*

[f] *Columbia University, New York, NY, 10027, USA*

[g] *Fermi National Accelerator Laboratory (FNAL), Batavia, IL 60510, USA*

[1] now at: Harvard University, Cambridge, MA, 02138, USA

[h] Illinois Institute of Technology (IIT), Chicago, IL 60616, USA
[i] Kansas State University (KSU), Manhattan, KS, 66506, USA
[j] Lancaster University, Lancaster LA1 4YW, United Kingdom
[k] Los Alamos National Laboratory (LANL), Los Alamos, NM, 87545, USA
[l] The University of Manchester, Manchester M13 9PL, United Kingdom
[m] Massachusetts Institute of Technology (MIT), Cambridge, MA, 02139, USA
[n] University of Michigan, Ann Arbor, MI, 48109, USA
[o] New Mexico State University (NMSU), Las Cruces, NM, 88003, USA
[p] Otterbein University, Westerville, OH, 43081, USA
[q] University of Oxford, Oxford OX1 3RH, United Kingdom
[r] Pacific Northwest National Laboratory (PNNL), Richland, WA, 99352, USA
[s] University of Pittsburgh, Pittsburgh, PA, 15260, USA
[t] Saint Mary's University of Minnesota, Winona, MN, 55987, USA
[u] SLAC National Accelerator Laboratory, Menlo Park, CA, 94025, USA
[v] Syracuse University, Syracuse, NY, 13244, USA
[w] Tel Aviv University, Tel Aviv, Israel, 69978
[x] University of Tennessee, Knoxville, TN, 37996, USA
[y] University of Texas, Arlington, TX, 76019, USA
[z] TUBITAK Space Technologies Research Institute, METU Campus, TR-06800, Ankara, Turkey
[aa] Center for Neutrino Physics, Virginia Tech, Blacksburg, VA, 24061, USA
[bb] Yale University, New Haven, CT, 06520, USA

Abstract: The low-noise operation of readout electronics in a liquid argon time projection chamber (LArTPC) is critical to properly extract the distribution of ionization charge deposited on the wire planes of the TPC, especially for the induction planes. This paper describes the characteristics and mitigation of the observed noise in the MicroBooNE detector. The MicroBooNE's single-phase LArTPC comprises two induction planes and one collection sense wire plane with a total of 8256 wires. Current induced on each TPC wire is amplified and shaped by custom low-power, low-noise ASICs immersed in the liquid argon. The digitization of the signal waveform occurs outside the cryostat. Using data from the first year of MicroBooNE operations, several excess noise sources in the TPC were identified and mitigated. The residual equivalent noise charge (ENC) after noise filtering varies with wire length and is found to be below 400 electrons for the longest wires (4.7 m). The response is consistent with the cold electronics design expectations and is found to be stable with time and uniform over the functioning channels. This noise level is significantly lower than previous experiments utilizing warm front-end electronics.

Keywords: Cold Electronics; Noise; MicroBooNE; Time projection chambers; Noble liquid detectors; Neutrino detectors

Contents

1 Introduction

The liquid argon time projection chamber (LArTPC) [1–4] is a totally active three-dimensional (3D) tracking calorimeter that enables the detection of accelerator neutrinos, supernova burst neutrinos, and sensitive searches for proton decay, with unprecedented spatial resolution for detectors of this scale.

The MicroBooNE detector, a 170 ton LArTPC, commenced operations in the Booster Neutrino Beam in October 2015. During an initial operating period from October 2015 through July 2016, several distinct types of TPC noise were observed in the MicroBooNE data which exceeded expectations for the types of noise inherent to the electronics. Characteristics of the noise in the

frequency and time domains were determined, and tests to identify the possible sources of the excess noise were performed. An offline noise filter was developed that eliminates most of the excess noise while retaining excellent signal preservation. The filtered noise levels are consistent with expected irreducible noise inherent to the cold front end application-specific integrated circuits (ASICs) and the analog-to-digital converters (ADCs).

In summer of 2016, several hardware upgrades were performed to mitigate the two largest sources of excess noise. After the successful upgrade, the residual excess noise was largely diminished reducing the requirement for offline filtering.

Details are presented in this paper as follows: section 3 describes the basic design features and the inherent noise of the readout electronics. Section 4 describes the status of the TPC readout after installation. The details of the observed excess TPC noise in MicroBooNE, the corresponding offline noise filter, and impact of the noise filter on the real signals induced by ionization charge are described in section 5. Section 6 describes the residual noise level after the noise filter was implemented and section 7 presents a metric to compare peak-signal from minimum ionizing tracks observed in data with the measured noise. Hardware upgrades to mitigate the two largest sources of excess noise and their effect are summarized in section 8. The conclusions and outlook are summarized in section 9.

2 MicroBooNE detector and readout electronics

The MicroBooNE detector [5] is a recently built LArTPC designed to observe interactions of neutrinos from the on-axis Booster [6] and off-axis NuMI [7] neutrino beams at the Fermi National Accelerator Laboratory in Batavia, IL. The detector consists of a 2.56 m$\times$2.32 m$\times$10.36 m TPC for charge detection, and an array of 32 photomultiplier tubes (PMTs) [8] that detect scintillation light for triggering, timing, and reconstruction purposes. The active mass of the detector is 85 metric tons of liquid argon (LAr). The TPC is housed in a foam-insulated evacuable cryostat vessel with a 2.56 m drift distance bounded on one end by the cathode plane and the other by three parallel anode wire readout planes. In the drift direction, these planes are labeled "U", "V", and "Y". The U, V, and Y planes contain 2400, 2400, and 3256 wires, respectively. The wire spacing within a plane is 3 mm, and the planes are spaced by 3 mm. The wires comprising the Y plane run vertically and the wires in the U and V planes are oriented $\pm 60^\circ$ with respect to vertical. While the TPC cathode is designed to operate at a high voltage (HV) of -128 kV, corresponding to a drift electric field of 500 V/cm, MicroBooNE currently operates at -70 kV, corresponding to a drift field of 273 V/cm. In this field, the ionization electrons drift at a speed of 1.114 mm/μs [9].

Figure 1 illustrates the signal formation in the MicroBooNE TPC. The ionization electrons produced along an energetic charged particle track drift through the LAr along the electric field lines toward the anode wire planes. Bipolar currents are induced on the wires of the U and V planes, commonly referred to as the *induction planes*, as the charge drifts towards and then past them. A unipolar signal is induced on a wire of the Y plane or *collection plane*, as all nearby ionization is collected. In addition, there are second order effects due to long range induction that contribute to the induced current waveform on any given wire [10, 11]. Bias voltages for the U, V and Y planes, -110 V, 0 V, and 230 V, respectively, are applied to each wire plane to ensure the two induction

planes satisfy the transparency condition [12] that all drifting electrons pass by the induction plane wires and fully collect on wires in the last (collection) plane.

Figure 2 illustrates the digitized simulated signal waveforms on the induction and collection planes assuming an ideal minimum ionizing particle (MIP) track. Since the ionization electrons are collected by the Y plane wires, integrating the waveform recorded from each Y wire gives a measure of the charge deposited along that section of the track. The peaks of the bipolar signals on the U and V induction wires are typically a factor of 2 to 3 smaller than the peak of the unipolar signal on the Y collection wires for this kind of signal.

The requirements on the TPC readout electronics performance are driven by the physics goals of MicroBooNE. The dynamic range and noise performance of the TPC readout are determined by the need to clearly measure the ionization charge arriving at the wire planes for a range of activity varying from the small charge created by a MIP to the large ionization deposited by stopping protons emerging from the breakup of an argon nucleus [13].

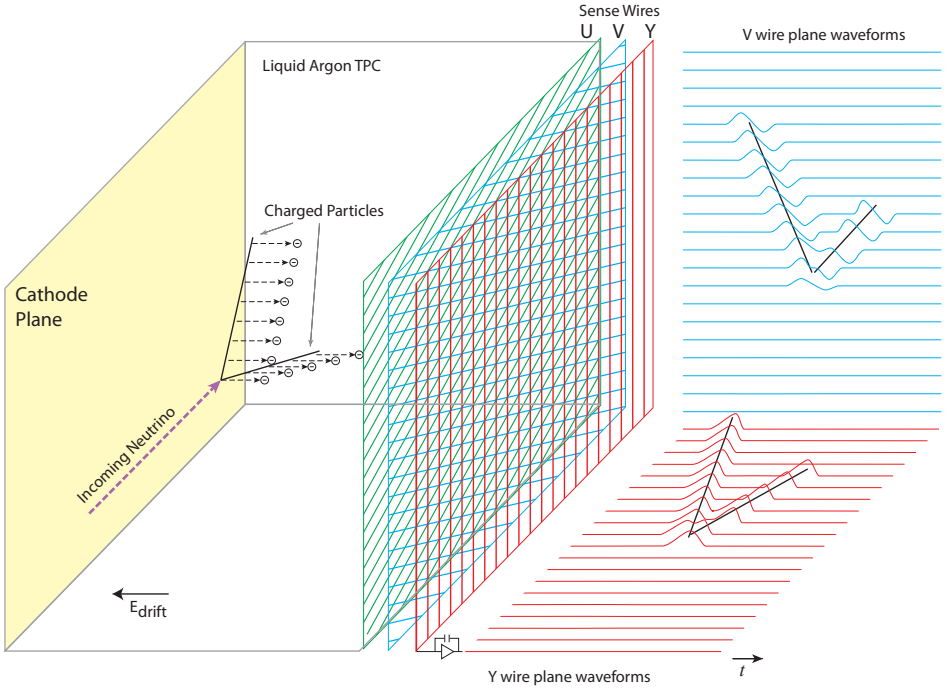

Figure 1. Diagram illustrating the signal formation in a LArTPC with three wire planes [5]. For simplicity, the signal in the first U induction plane is omitted in the illustration. Planes are positioned in the order U, V, Y with the Y plane being farthest from the cathode plane.

The induced current on each wire is amplified and shaped through one dedicated channel (out of 16) of a custom designed complementary metal-oxide-semiconductor (CMOS) analog front-end cold ASICs [15]. The analog front-end ASICs, which include a pre-amplifier, shaper, and signal driver are located inside the cryostat along with the wire bias voltage distribution system, decoupling

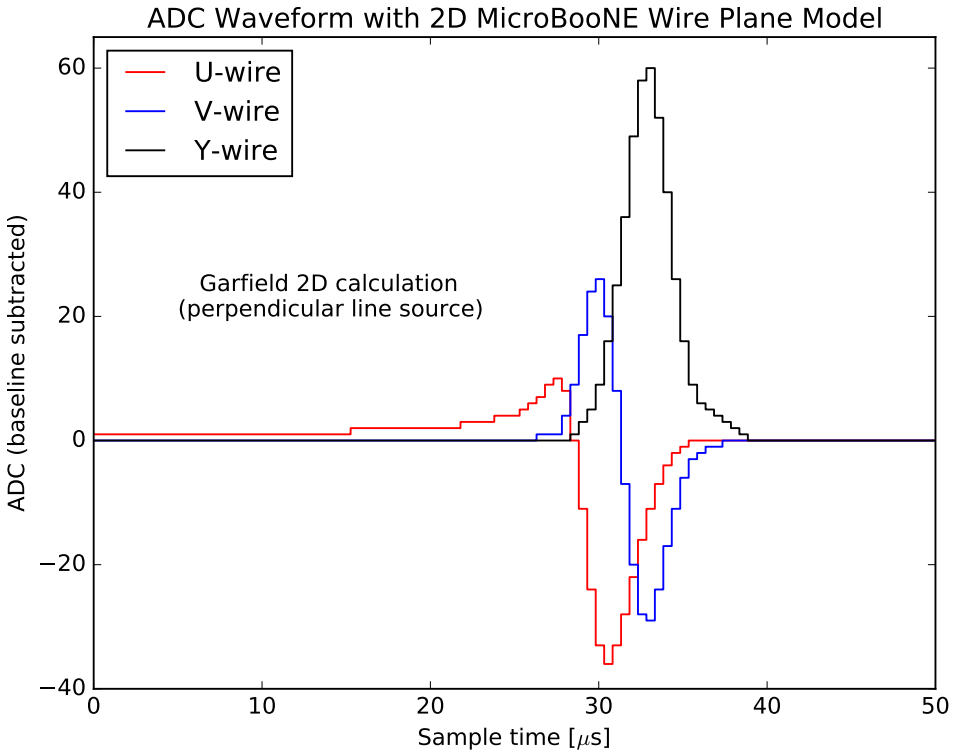

Figure 2. The digitized signals from a central wire from each plane that are induced by an ideal MIP track in a 2D model of the MicroBooNE TPC. The high resolution field response functions used were calculated with Garfield 2D [14]. They were defined on drift paths spaced by 10% of the pitch which cover ten wires to either side of the three central wires. An electronics response function with an amplifier gain of 14 mV/fC and peaking time of 2 µs is used to model the ASIC and an additional gain of 1.2 is used to account for subsequent amplification stages. The track is an ideal line source that runs perpendicular to all wires, consists of 5300 ionization electrons per mm and spans the transverse domain of the calculation.

capacitors, and calibration networks. HV capacitors of 2.2 nF rated to 1 kV and 4.7 nF rated to 630 V are mounted on the wire carrier base boards [16] to AC-couple the Y and U wires to the readout electronics. Current-limiting resistors of 22 MΩ are placed between the bias voltage bus and each wire in case a wire is shorted to a different wire plane. V wires do not have HV bias resistors or decoupling capacitors, as they are DC coupled to the readout electronics. A set of ASICs is mounted on one front-end motherboard (FEMB), which is placed close to the end of the sense wires, embedded inside the LAr in order to minimize the capacitive load - and hence noise - into the ASICs. As will be discussed in section 3, the cold temperature further reduces the noise with respect to the room temperature operation of these ASICs.

The ASICs can operate at one of four gain settings (4.7 mV/fC, 7.8 mV/fC, 14 mV/fC and 25 mV/fC). The gain determines the peak height of the output voltage waveform because of the collection of an impulse of unit charge. Four peaking time settings (0.5 µs, 1.0 µs, 2.0 µs and 3.0 µs) are available. The peaking time is defined as the time difference between 5% of the peak position and the signal peak of an impulse response. The ASICs are nominally operated at 14 mV/fC gain

and 2 µs peaking time settings throughout data taking.

The output dynamic range of the cold ASIC is 1.6 V. The output signals from the ASICs are transmitted over of distance of 2.5 m to 5.5 m by twisted-pair copper cable, through a warm flange, and to an intermediate amplifier line-driver which resides in an enclosure that forms a Faraday cage with the cryostat. The intermediate amplifiers compensate for losses incurred by the signals as they are then driven over 10 m of shielded, twisted-pair cables to the data acquisition (DAQ) TPC readout boards in crates on the platform above the detector. At this point, these signals having picked up a gain of 1.2 are digitized by AD9222 [17] ADCs.

The ADC has a dynamic range of 2 V, digitizes with a sampling rate of 2 MHz, and records 12 bit samples with an inherent ADC noise that gives an effective number of bits of 11.3 [18]. In order to match the output voltage range of the cold ASIC and the input range of the ADC, a resistor-capacitor (RC) circuit with 1 ms time constant is included in the intermediate amplifier to remove the ASIC baseline voltage. The intermediate amplifier and receiver/ADC board provides the net gain of 1.2 to the signal helps match the differing voltage ranges of the cold ASIC and ADC. A second RC circuit with a 1 ms time constant is installed in front of the ADC to make the ADC pedestal[1] independent of the intermediate amplifier baseline.

Each DAQ readout window is 4.8 ms in duration, which corresponds to 9600 recorded samples (also called time ticks or ticks), and is slightly more than twice the time needed for an ionization electron to drift the full width of the detector. The digitized signal from the ADC module is passed directly to a field-programmable gate array (FPGA) chip for initial data processing, data reduction, and preparation for readout by the DAQ system. A schematic of the MicroBooNE readout electronics is shown in figure 3.

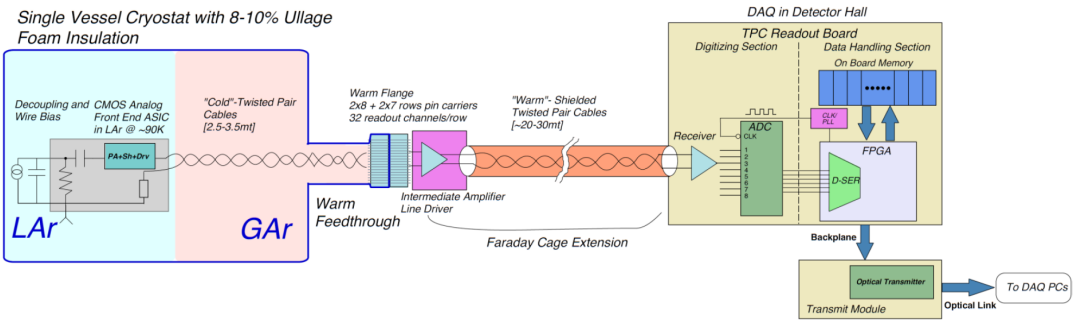

Figure 3. Schematic of MicroBooNE cold and warm electronics readout chain [13]. See text for more explanation.

3 Front-end readout electronics response and inherent noise

To better understand the overall electronics response and the inherent noise of the MicroBooNE readout electronics, the entire front-end electronics chain up to the ADC can be described in terms of four basic circuits:

1. A charge pre-amplifier in the cold ASIC.

[1]The pedestal value of the ADC output is an effective offset. It is defined by the integration of the excess signal from the gate pulse which allows current to pass into the ADC.

2. A subsequent shaping circuit in the cold ASIC.

3. An RC circuit in the intermediate, line-driver amplifier.

4. A pedestal-adjusting RC circuit located just before the ADC input.

3.1 Impulse response

As described earlier, the analog signal from the MicroBooNE front-end electronics is digitized by a 12 bit ADC with a sampling rate of 2 MHz. According to the Nyquist theorem [19], the information in a continuous signal is fully sampled if the signal contains no power at frequencies above the Nyquist frequency of one-half the sampling rate. The MicroBooNE pre-amplifier and shaper are therefore designed to provide an anti-aliasing filter that restricts the frequency content of the analog signal to frequencies below the frequency of 1 MHz. The MicroBooNE anti-aliasing filter is based on a fifth order, low-pass network designed to obtain an impulse response close to a Gaussian distribution in the time domain. The impulse response function in the time domain is obtained from the inverse Laplace transformation of the transfer function for the network

$$T(s) = \frac{A_0 \cdot C_A}{(p_0 + s) \cdot (p_{i1}^2 + (p_{r1} + s)^2) \cdot (p_{i2}^2 + (p_{r2} + s)^2)}, \tag{3.1}$$

with s being a complex frequency variable. The parameters in equation 3.1 are obtained from a detailed simulation of the network design and are determined to be:

$$\begin{aligned} p_{r1} &= \frac{1.417}{t_p \cdot C_T}, \quad p_{r2} = \frac{1.204}{t_p \cdot C_T}, \\ p_{i1} &= \frac{0.598}{t_p \cdot C_T}, \quad p_{i2} = \frac{1.299}{t_p \cdot C_T}, \\ p_0 &= \frac{1.477}{t_p \cdot C_T}, \quad C_A = \frac{2.7433}{(t_p \cdot C_T)^4}, \\ C_T &= \frac{1}{1.996}; \end{aligned} \tag{3.2}$$

where A_0 is the gain parameter and t_p is the peaking time constant. $T(s)$ has units of $\frac{\mathrm{V}}{\mathrm{C}}\ (\mathrm{Hz})^{-1}$.

The impulse response function in the time domain is shown in figure 4. The front-end cold electronics are programmable with four different gain settings (4.7 mV/fC, 7.8 mV/fC, 14 mV/fC and 25 mV/fC) and four peaking time settings (0.5 µs, 1.0 µs, 2.0 µs and 3.0 µs). For a fixed gain setting, the peak of the impulse response is always at the same height independent of the peaking time. The different gain settings allow for use in applications with differing ranges of input signal strength. The four peaking time settings are provided to satisfy the Nyquist criterion at different sampling rates. More details on peaking time and gain optimization can be found in section 3.2. A calibration capacitor of 183 fF is installed in the ASIC to allow for a calibration of the electronic response for every channel. Given the overall output dynamic range of 1.6 V (the shape of the impulse response function is shown in figure 4) and the expected level of intrinsic noise, the baselines chosen for the collection plane and the induction plane (bipolar signals) are ≈200 mV and 900 mV respectively. From the test stand and in-situ pulser measurements, it was observed that

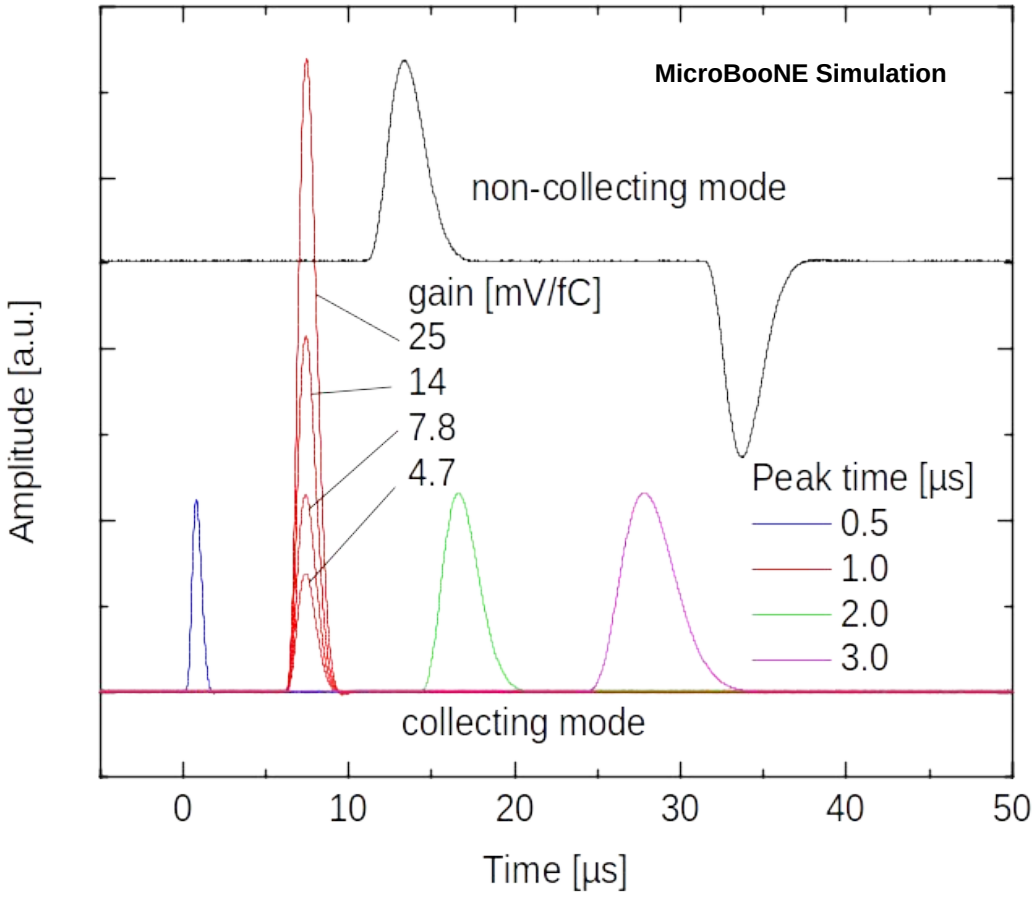

Figure 4. ASIC impulse response functions are shown for four peaking times and four gain settings. The example of a calibration pulse (black curve) through injecting a rectangular wave is also shown. Vertical axis units (a.u.) are equivalent to mV/fC. The baseline setting is ≈200 mV for collecting mode and 900 mV for non-collecting (induction) mode.

the channels with a baseline of 900 mV have ≈3% lower gain than the channels with a baseline of 200 mV.

For the two RC circuits, the resulting total electronics response is a convolution of their individual RC response functions: $R_{RC}(t) = \delta(t) - (e^{-t/t_0}/t_0)$ with $t_0 = 1$ ms. These RC circuits introduce long tails to the impulse response that may lead to distortions in reconstructed ionization charge distributions along the drift direction. Since the time constant is generally long (1 ms) with respect to the duration of a typical signal, the effect of this response function is negligible for most signals. However, in the case of a large amplitude signal with a long duration (for example, a long, vertical cosmic muon track that is almost parallel to the collection wires), the effect of the RC circuits is visible. Figures 5(a) and 5(b) show the signal before and after correcting for the RC shaping effect through the deconvolution process [20]. Such a correction is generally effective in removing this type of distortion. There are certain scenarios where such a correction would fail. For example, if the signal from a vertical cosmic muon arrived just before the 4.8 ms readout time,

the recorded data would miss the primary signal that is large and positive, and would only include a long negative tail. Failing to account for this effect would lead to a significant baseline distortion for its few occurrences. Instead, such signals are identified by examining the very low frequency amplitudes and, where identified, the slowly varying baseline under these signals is directly removed in the time domain.

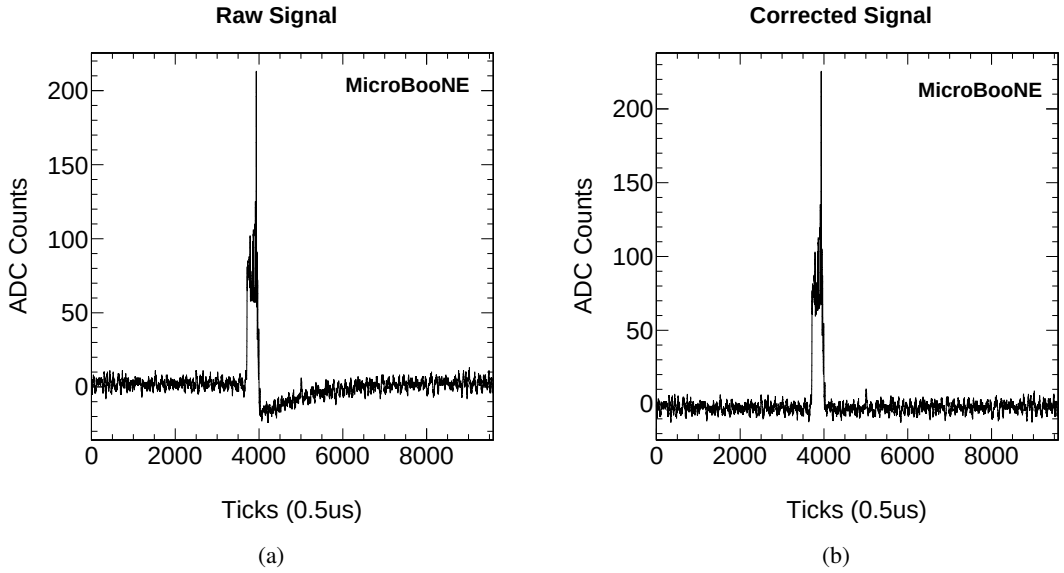

Figure 5. Example Y plane raw signal waveforms from data: (a) before correcting, and (b) after correcting for the RC shaping effect. This signal corresponds to a cosmic muon traveling close to parallel to the collection wires.

3.2 ASIC operation optimization

Some flexibility to optimize the ASIC operation in-situ is allowed by the ability to select among the four gain and four peaking time settings provided by the cold ASIC. There are two considerations when determining the optimal gain setting. The gain must be chosen low enough to ensure a large signal, such as from many highly ionizing protons exiting a neutrino interaction vertex over a small volume, does not saturate the pre-amplifier. On the other hand, the gain must be large enough to allow small signals, such as from MIP track after undergoing both electron diffusion and absorption across a large drift, to be well above the gain-independent noise from sources beyond the pre-amplifier (e.g., noise associated with the intermediate amplifier). The nominal gain setting for MicroBooNE is 14 mV/fC. The saturation limit is more than 45 times larger than the signal due to a MIP traveling parallel to the wire plane and perpendicular to the wire orientation, and more than seven times larger than the signal due to a stopping proton. This estimation assumes negligible charge attenuation during the drift. With this setting, the electronics noise from the intermediate line-driver amplifier and the ADC is expected to be negligible compared to the inherent noise associated with the cold ASICs.

Criteria for selecting an optimum peaking time, and ADC sampling rate are related, as the choice determines the amount of resulting noise. The peaking time determines the level of detail

of the original input signal that is retained while the sampling rate determines how accurately that remaining detail is recorded. This means that, for best waveform reproduction accuracy, the optimum choice for the peaking time should scale inversely with the optimum choice for the sampling rate. As will be discussed in section 3.3, the peaking time also impacts the inherent noise from the pre-amplifier and shaper. An optimization of the peaking time and the sampling rate therefore affects both the accuracy with which the signal can be measured, and the signal-to-noise performance of the readout electronics.

Given the continuous nature of a realizable low-pass filter there is a necessary trade-off between the amount of bandwidth the filter passes and the amount of aliasing it allows. Either the filter attenuates frequencies below the Nyquist frequency, or it allows some power above the Nyquist frequency leading to some aliasing. For MicroBooNE, we chose to avoid aliasing and *oversample* at a rate higher than strictly required to cover the bandwidth of the filter. Oversampling is defined as

$$M = \frac{f_N}{f_{NR}} = \frac{f_s}{4 f_{3db}}, \tag{3.3}$$

where f_N is the Nyquist frequency and f_{NR} is the frequency beyond which the power of signals is negligible after applying the anti-aliasing filter. f_s is the sampling rate with $f_N{=}f_s/2$ and f_{3db} is the frequency where the response of the anti-aliasing filter is reduced by 3 dB. The cut-off frequency of the signal f_{NR} is then estimated to be $2 f_{3db}$.

In MicroBooNE, the sampling frequency is 2 MHz and the shortest peaking time for the anti-aliasing filter sufficient to provide high accuracy charge measurement is therefore $t_p = 1$ µs. For the filter response described by equation 3.1, $f_{3db} \approx 0.25$ MHz, resulting in oversampling of $M = 2$. In principle, samples taken after longer anti-aliasing filters (peaking time ≈2 µs, 3 µs and higher) contain progressively less and less information about the finer features of the induced current waveforms. The optimum choice of the sampling frequency and corresponding peaking time is ultimately determined by the time scale of the induced currents, i.e., by the electron drift velocity, wire plane spacing, and diffusion. In MicroBooNE, the peaking time was chosen to be 2 µs instead of 1 µs due to the chosen drift field. The lower drift field leads to slower electron drift which has two effects on the inherent time spread of signals. First, it leads to a longer feature size of the signal due to a longer drift near the wire planes. Second, drifts require more time on average, allowing for more diffusion which again leads to smoother signal features. All together, little information is lost with a 2 µs peaking time, and this has the advantage of a slightly lower inherent noise than the 1 µs setting as discussed in the following section.

3.3 Front-end ASIC inherent noise

In this section, we describe the inherent noise associated with the front-end ASIC. The major components of this irreducible noise are:

- Series noise associated with the gain mechanism in the first transistor of the charge pre-amplifier. It consists of two components:
  - a "white series" noise due to thermal fluctuations in the input transistor,
  - a "$1/f$ series" noise (sometimes referred to as "pink" noise) due to charge trapping and de-trapping in the input transistor. The $1/f$ noise dominates at low frequencies.

- "white parallel" noise due to the transistor bias current and resistors providing wire bias voltage.

- "f parallel" noise which arises from thermal fluctuations in the dielectric components such as the circuit boards and wire carrier boards. Upon integration on the input capacitance this noise acts as a series $1/f$ noise [21]. By design, this noise is much lower than other sources.

The level of noise from the entire electronic readout chain is expressed as the equivalent noise charge (ENC) measured in units of number of electrons. The ENC is defined as the number of instantaneously collected electrons required so that their peak ADC count is equal to the root mean square (RMS) of the noise measured, also in the units of ADC counts. The ENC from the noise sources listed above can be approximated as [21, 22]:

$$\mathrm{ENC}^2 \approx \frac{1}{2} A_1 \frac{e_n^2 C_{in}^2}{t_p} + A_2 \pi C_{in}^2 A_f + A_3 \left(q_e I_o + \frac{2 k_B T}{R_b} \right) t_p, \tag{3.4}$$

The first two terms represent the white and $1/f$ series input transistor noise. Here, C_{in} is the total capacitance at the input of the ASIC, which includes that of the sense wire, the leads, their connections to the ASIC and the input transistor gate capacitance. Here, e_n is the white series noise spectral density in the unit of V/Hz. The series $1/f$ noise spectral density in $\mathrm{V}/\sqrt{\mathrm{Hz}}$ is given by $\sqrt{A_f/f}$. Both e_n and A_f are determined from the ASIC's input p-channel metal-oxide semiconductor (pMOS) transistor measurements and depend on the transistor technology and transistor design (optimization of transistor electrode dimensions and operating conditions as described in reference [23]). The two components in the third term represent white parallel noise, arising from the ASIC bias current, I_o (shot noise) and the wire bias resistor (thermal noise), where k_B is the Boltzmann constant, q_e is electron charge, T is temperature and R_b is resistance of the wire bias resistor. The t_p in equation 3.4 is the peaking time of the anti-aliasing filter. The dimensionless form coefficients for the semi-Gaussian impulse response functions, such as given by equation 3.1 and 3.2, are A_1=2.0, A_2=0.9 and A_3=1.0 [21].

At temperatures of 77 K to 89 K, charge carrier mobility in silicon increases and thermal fluctuations decrease with $k_B T/q_e$. This results in higher gain, higher speed, and lower noise. The series $1/f$ noise and CMOS transistor white series noise amplitude, e_n at 77 K is a factor of 2 lower than at 300 K. Therefore, operation of the front-end ASIC at LAr temperatures significantly reduces the inherent noise. The ASIC has been designed to minimize the white parallel noise by limiting the bias current; the lower limit has to be set so as to avoid pre-amplifier saturation by the currents induced by sense wire motion (section 4.3). Therefore, the ENC due to the first transistor noise is the dominant noise source in the cold ASIC [15, 23]. For peaking times $>$ 1 µs, the ASIC noise at 77 K is dominated by $1/f$ noise from the first transistor. For a capacitance of 220 pF connected to the input, and the peaking time of 2 µs, the total ASIC ENC measured is ≈550 electrons at 77 K [24]. Out of this, only ≈150 ENC is from white parallel noise. These results are in good agreement with the expectation from the simulation as shown in figure 6.

The capacitance of the sense wires contribute substantially to the input capacitance C_{in} and dominates in the case of the longest wires. Two estimates of wire capacitance are given here. The first follows reference [25] in the case of a parallel wire grid, symmetrically placed between two

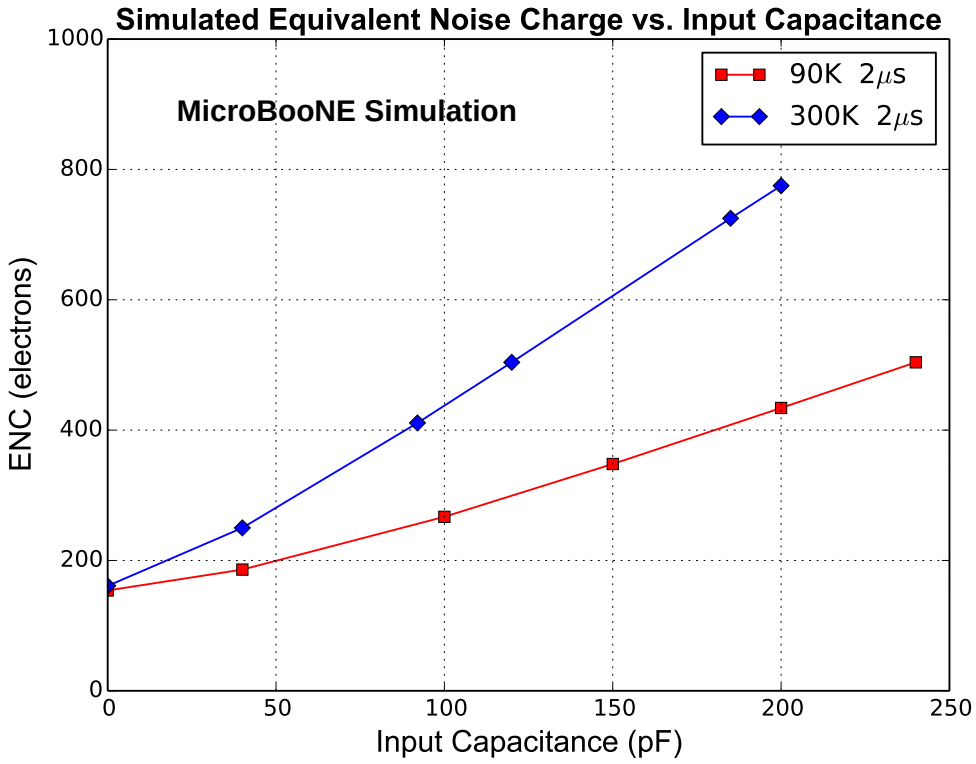

Figure 6. Simulated equivalent noise charge vs. input capacitance for $T = 90$ K (red) and $T = 300$ K (blue).

conducting planes. The capacitance per length C_{wire} is given by:

$$C_{wire} = \frac{2\pi\epsilon_o\epsilon_r}{(\pi G/W) - \ln(\pi d/W)}, \tag{3.5}$$

where ϵ_0 is the permittivity of free space, ϵ_r is the relative dielectric constant for liquid argon, W is the wire spacing, G is the plane gap, and d is the wire diameter. For MicroBooNE's wire spacing and 150 µm wire diameter, this corresponds to a capacitance per unit wire length of ≈17 pF/m. This number is expected to be smaller than its actual value since equation 3.5 assumes an electrode geometry of parallel wires between two parallel plates, instead of the actual multiple wire plane geometry. The second estimate is based on a 2-D finite-element analysis [26] and yields a capacitance value of ≈20 pF/m for U and Y wire plane and 21 pF/m for the middle V wire plane.

From equation 3.4, a general formula characterizing the observed front-end readout noise level as a function of wire length in terms of RMS ADC counts can be written as:

$$\text{ENC} \propto \text{Noise}_{\text{RMS}}\ (\text{ADC}) = \sqrt{\text{x}^2 + (\text{y} + \text{z} \times \text{L})^2}, \tag{3.6}$$

where x corresponds to the third term in equation 3.4 and is due to the white parallel noise, and noise from front-end readout components other than the ASIC, such as the noise associated with the intermediate amplifier and the ADC. The second term is due to the series noise, with y arising from noise due to the transistor gate capacitance and capacitance of the wire-to-ASIC connections.

The last term is due to the wire capacitance, which is proportional to the wire length L. All terms are expressed in ADC units. As discussed in the previous sections, the noise from components other than the cold ASICs in the front-end readout chain is inversely proportional to the overall gain prior to the ADC when converted into ENC.

Finally, the inherent ADC noise, including quantization noise, is such that it provides an equivalent number of bits of 11.3. This corresponds to a noise level of $\sigma = 1.6 \times (1/\sqrt{12}) \approx 0.46$ counts of the 12 bit ADC.

In the following sections, we describe the status of TPC readout, characteristics of the excess noise seen in MicroBooNE TPC, and a comparison with the expected inherent noise.

4 Status of the TPC readout post-installation

A study of the status of the TPC readout channels in MicroBooNE was conducted after installation and filling of the cryostat with liquid argon. The pedestal distribution during regular data taking and the ASIC impulse response using calibration data taken with the external pulser are used to identify both operational and non-functioning channels. It was discovered that ≈10% of the channels were non-functional.[2] In the following sections, the causes of various channel failures are detailed. The operational status of the channels are taken into account in the further steps in data analysis.

4.1 Misconfigured channels

The 8256 channels reading out the MicroBooNE TPC are grouped into 516 ASICs [27] (16 channels per ASIC). As discussed in section 3.2, the gain and peaking time settings for the ASICs during production data taking were selected to be 14 mV/fC and 2 µs, respectively. By analyzing raw data in the time and frequency domain and using the pulser calibration signals to determine the gain, it was found that 14 ASICs (224 channels) were instead consistent with the factory settings of a gain of 4.7 mV/fC and a peaking time of 1 µs. All of these channels read out the first induction (U) plane. The cause of this mis-configuration is believed to be due to damage to the configuration signal lines on these ASICs from electrostatic discharge (ESD) during detector installation.

Since the expected electronic noise characteristics are different for different peaking times, these misconfigured channels can be identified in the frequency domain. As shown in figure 7, the average frequency content of signals recorded by channels with a 2 µs peaking time is clearly different from that of channels with a 1 µs peaking time. The higher peaking time acts as a low pass filter, removing the highest frequency components. The relative difference in the heights of the two low frequency peaks are evident and consistent with the two gain and peaking time settings as well as the noise from non-ASIC sources (e.g., the ADC and line-driver amplifier).

Although these channels are misconfigured, they are usable because a signal can still be discerned from the electronic noise. The shaping produced by the misconfigured settings (4.7 mV/fC and 1 µs) is corrected by the shaping corresponding to the intended settings (14 mV/fC and 2 µs). This correction is done through an offline noise filter that allows the waveforms from these channels to be treated in the same manner as those from other channels by the procedures that are applied later in the analysis chain.

[2] For event reconstruction using two wire planes, the resultant inefficiency is estimated to be ≈3%.

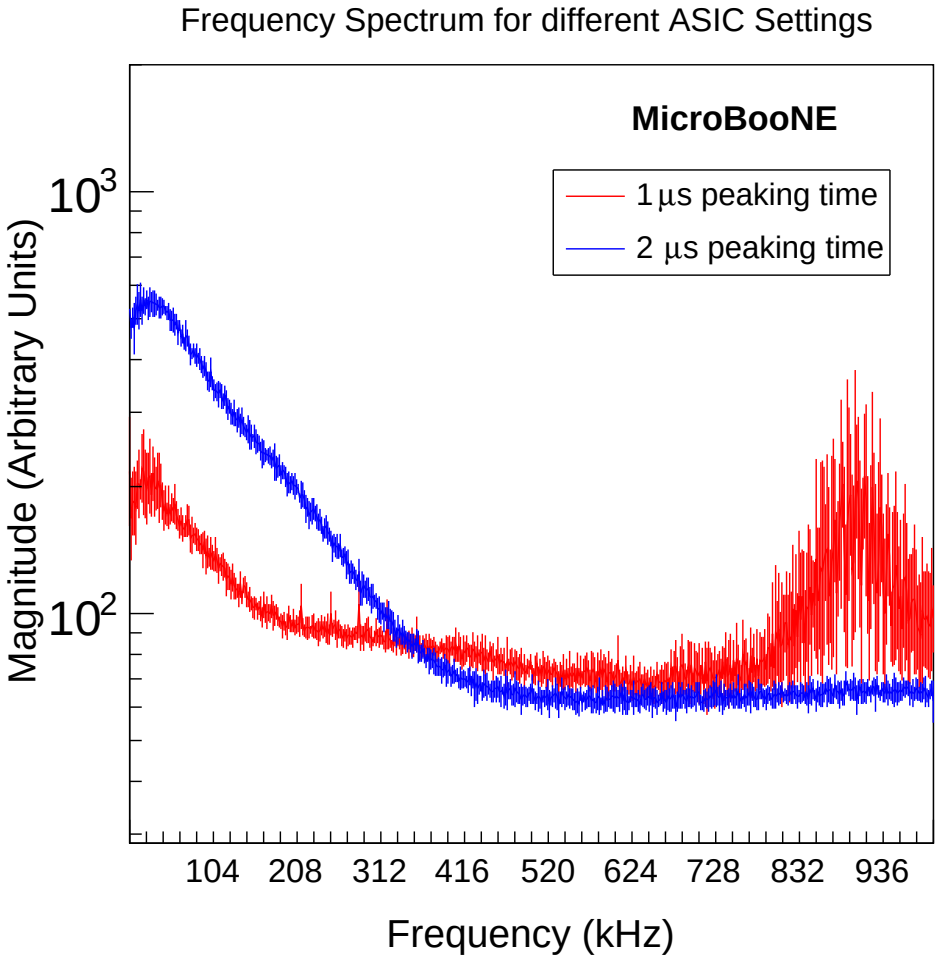

Figure 7. The average frequency domain magnitude for channels with 1 µs peaking time and 4.7 mV/fC gain (red) and with 2 µs peaking time and 14 mV/fC gain (blue). The magnitude represents the amplitudes of various frequency components. The average is taken over ≈200 U plane channels and has smoothed out random factors associated with the noise spectrum for individual channels. The peak ≈900 kHz for the 1 µs setting is due to the high frequency burst noise described in section 5.3.

The misconfigured channels are associated with larger noise than the other channels. First, the 1 µs peaking time setting leads to ≈10 % higher inherent ASIC noise compared to the 2 µs peaking time [24] (see section 6). More importantly, as discussed in section 3.2, the lowest gain setting leads to a much larger relative contribution of the electronics noise originating downstream of the cold ASIC from the intermediate amplifier and the ADC.

4.2 Shorted channels

At the start of the commissioning, all wire bias voltage lines were tested and exhibited the expected high resistance to ground (in the GΩ range). The sense wire bias voltage is supplied to the wires through the signal feedthroughs [13]. Upon application of the bias voltage, three signal

feedthroughs started drawing more current than the voltage source could supply. In coincidence, the noise increased on a number of U channels by a factor of ≈20 and the external pulser signal was reduced by ≈30%. An anomalous response was also observed on a single V plane channel.

These observations could be explained by a single V wire coming in contact with a number of U wires, thus establishing a DC electrical contact across different feedthroughs. The diagnosis by DC measurements was facilitated by the wire bias distribution arrangement. Each U or Y wire receives its bias voltage via a 22 MΩ resistor. On the other hand, each V wire has zero bias as it is connected directly to the protection diodes at the input to the ASIC. Thus, a measurement of the current vs. bias voltage at the feedthrough indicates how many 22 MΩ resistors appear connected in parallel. This number is interpreted to be the number of U wires from a particular feedthrough that are in contact with the V wire. The derived number of shorted wires during production data taking is consistent with the 287 non-functioning U channels, of which 259 channels have no signal and 28 channels have a high level of noise.

These U wires are not expected to retain their bias voltage and thus disturb the nearby electric field. As a result, some amount of drifting ionization electrons that would otherwise pass by these U wires is instead expected to be collected on them. This leads to a smaller signal amplitude in the subsequent nearby V and Y wires. This behavior is confirmed from analysis of the TPC signals from these channels. The MicroBooNE detector is welded shut making it impossible to easily access the interior of the cryostat for any diagnostics. A visual scan on the TPC wire plane was immediately performed [28]. However, as no direct contact between the V and U wires was observed, the exact location of the short is not known at the moment of writing of this paper.

Beside these U wires, there is a group of Y wires that are identified to be shorted to ground through the leakage current for a bias voltage power supply. As a result, the ionization electrons that would otherwise be collected by these Y wires are instead collected by the V wires crossing in front of them. This was confirmed by observing unipolar signals in these V wires instead of the expected bipolar signal. Signals from ionization electrons passing by V wires at locations distant to the grounded Y wires do produce the expected bipolar induction signals. This indicates that the problems arising from the grounding of the Y wires are local to these wires and do not extend to the entire length of the crossing V wires. The exact cause of this short is also not known at the writing of this paper.

4.3 Periodic saturation of ASICs

During the initial commissioning period of the MicroBooNE TPC, ≈10–15% of the induction planes channels were observed to display a periodic "saturation" behavior whereby the channel would be essentially non-functional for a period of time and then recover.

Figure 8(a) shows a waveform from an ASIC channel that has become saturated for part of the readout window. The saturation behavior is characterized by very low gain, low noise and no response to the external pulser. Some time after saturation the channel recovers to a normal state. Just after making a gross recovery, there is a period when the baseline is distorted due to the RC circuits as described in section 3. Saturation occurs sporadically and its incidence is higher when the wire bias voltage is higher. No saturation is seen for wires at zero bias voltage. Direct oscilloscope measurements at the output of the intermediate amplifier of several U and V channels that go into saturation indicate they do so with a distribution of average frequencies less than 15 Hz.

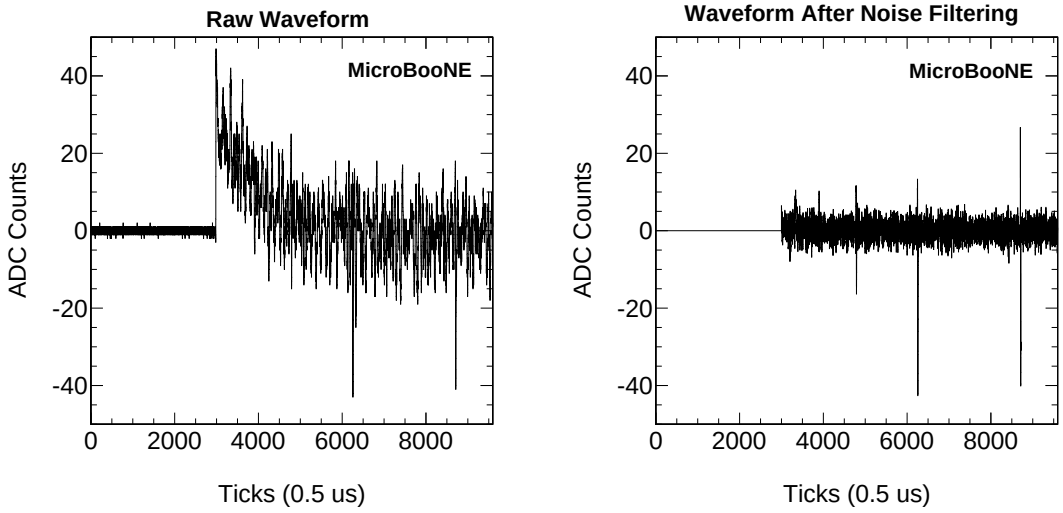

(a) (b)

Figure 8. An example V plane raw waveform: (a) after the recovery of an ASIC from saturation, and (b) the same waveform after the noise filter. In (a), the region corresponding to the ASIC saturation (low RMS region between 0 - 3000 Ticks) is clearly seen. In (b), the distortion of the baseline is removed by the noise filtering.

ASIC saturation occurs when a positive input current exceeds the bias current that keeps the ASIC input circuit in equilibrium. With a large positive current, the preamplifier is driven against its lower limit (near zero) and the signal gain becomes very low. This was confirmed by a dedicated bench test. The ASIC bias current should be maintained as low as possible as it contributes to the white parallel noise (shot noise) as discussed in section 3.3. The most likely cause of a large external current arises from the wire motion in the presence of an electric field.

A detailed study showed that, at low ASIC bias current settings, even a small wire displacement is sufficient to saturate the ASIC. For example, a V wire displacement of ≈100 µm (less than the 150 µm wire diameter) at frequencies in the range of 1 Hz to 20 Hz can induce a charge greater than 50 pC to saturate the ASIC that is biased at 100 pA.

One source of this saturation that has been considered and ruled out is a microphonic effect (noise due to mechanical vibrations). This source is unlikely cause as the damping provided by the liquid argon would not allow for any resonant excitation. Instead, more likely cause is convection of the liquid argon. Saturation is less likely on shorter wires because wire displacement is proportional to l^n, where l is wire length and $n = 2, 3$ depending on the displacement force distribution. This is consistent with the observed behavior.

The cold ASIC has two bias current settings (100 pA or 500 pA). As shown in equation 3.4, the bias current contributes to the overall noise level. The 100 pA setting is intended for short wires in induction wire planes as it gives a smaller shot noise. The 500 pA setting is the default setting for the majority of wires, which gives ≈80 and 110 ENC at 1 µs and 2 µs peaking time, respectively. During the initial MicroBooNE data taking, the ASIC bias current was inadvertently set to 100 pA. It was observed that a large fraction of channels on the induction planes (10-15%) and a few channels on

the collection plane experienced quasi-periodic saturation. After resetting the ASIC bias current to 500 pA, the incidence of saturation was reduced to a few tens of wires. The remaining intermittent saturation of the ASICs is time dependent and more details will be discussed in section 4.4.

Remaining saturation effects can be corrected offline. The identification of the saturation region in the offline data processing is based on finding that the local RMS of the pedestal is less than 1 ADC count within 20 time ticks. The regions of individual digitized signals corresponding to the saturation period are then identified on an event-by-event basis and the baseline distortion just after recovery is corrected. Figure 8(b) shows the waveform after applying an offline noise filter and removing the baseline distortion.

4.4 Summary and time dependence of non-functioning channels

The number and causes of the non-functioning channels in MicroBooNE are summarized in table 1. First, there are ≈20 channels that sporadically suffer from ASIC saturation after the reset of the bias current to 500 pA. The exact set of saturating channels varies with time since the saturation frequency varies for different channels, and changing detector conditions can change the liquid flow, which is suspected to cause the saturation. Second, 6 ASICs are not connected to TPC wires due to an installation error. Third, 19 ASICs cannot be initialized properly inside the liquid argon (so-called "start-up" problem). This issue is believed to be caused by the bandgap reference (BGR) circuit in the ASICs. A BGR is a temperature independent voltage reference circuit widely used in integrated circuits. It produces a fixed constant voltage regardless of power supply variations, temperature changes, and circuit load. For the ASICs with this start-up problem, the BGR circuit is suspected to be stuck in an incorrect initial state when the power supply ramps from 0 to 1.8 V. This is likely due to a larger transistor current in the cold than in the warm. Last, there are 126 Y channels with 116 channels having no signal and 10 channels with high noise located near the shorted wires between the V and Y plane and 287 U channels with 259 channels having no signal and 28 channels with high noise located near the shorted wires between the V and U planes. There are another 36 channels with high noise that have not been associated with shorted wires.

Table 1. Summary of the non-functioning channels for Run 3455 Event 6. A total of ≈862 channels are considered non-functioning. MB stands for front-end motherboard.

# non-functioning channels	Reason
≈20	ASIC saturation
96	6 ASICS on one MB not connected to wires
304	19 ASICs due to start-up problem
126	channels sorrounding U-Y shorted wires with 10 noisy channels
287	channels sorrounding U-V shorted wires with 28 noisy channels
36	noisy channels not located near the shorted wires

Finally, the time dependence of the total number of non-functioning channels is shown in figure 9. The operational status of the channels was checked over a period from February to July, 2016. Each data point in the figure is averaged over a ≈10 event sample from a given run. The number of non-functioning channels for the U and Y planes is stable except for a period at the start of

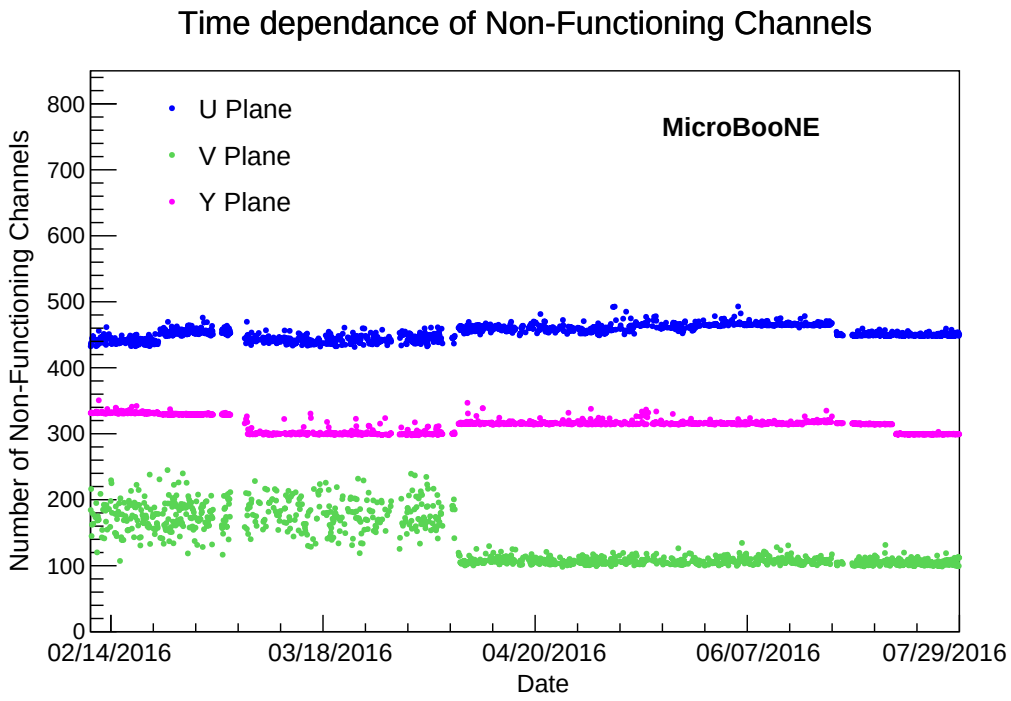

Figure 9. Average number of non-functioning channels taken over ≈10 events per run as a function of time.

March 2016. For a roughly one month period, the Y plane had a reduced number of non-functioning channels. This is due to the temporary recovery of two ASICs with the "start-up" issue that returned to a non-functioning state. Also shown in figure 9 is a decrease in non-functioning channels in V plane around the beginning of April. This is correlated with a replacement of a faulty cryogenic pump. After replacing the cryogenic pump, the occurrence of ASIC saturation became negligible. This fact suggests that the convection of the liquid argon might be the likely cause of saturation as described previously in section 4.3.

5 Identification and filtering of MicroBooNE TPC excess noise

In section 3.3, we described the noise inherent to the electronics. Excess noise, beyond the expected inherent noise, is observed in MicroBooNE. Figure 10(a) and 10(b) shows frequency spectra from U plane channels with different gains and peaking times to illustrate this excess noise. The excess noise is categorized into three types, ordered in decreasing importance:

- Noise induced by the low-voltage regulators: In section 5.1, the noise originating from the low-voltage regulators supplying the ASIC operating voltages is described. This noise is coherent across all the channels supplied by a regulator and shows up at the low end of the frequency spectrum ($\lessapprox 30$ kHz).
- Noise induced by the cathode high voltage power supply: In section 5.2, the noise induced on the anode wire plane by voltage fluctuations in the cathode potential, such as ripple from the HV supply is described. The two highest peaks are near 36 kHz and 108 kHz. The effect

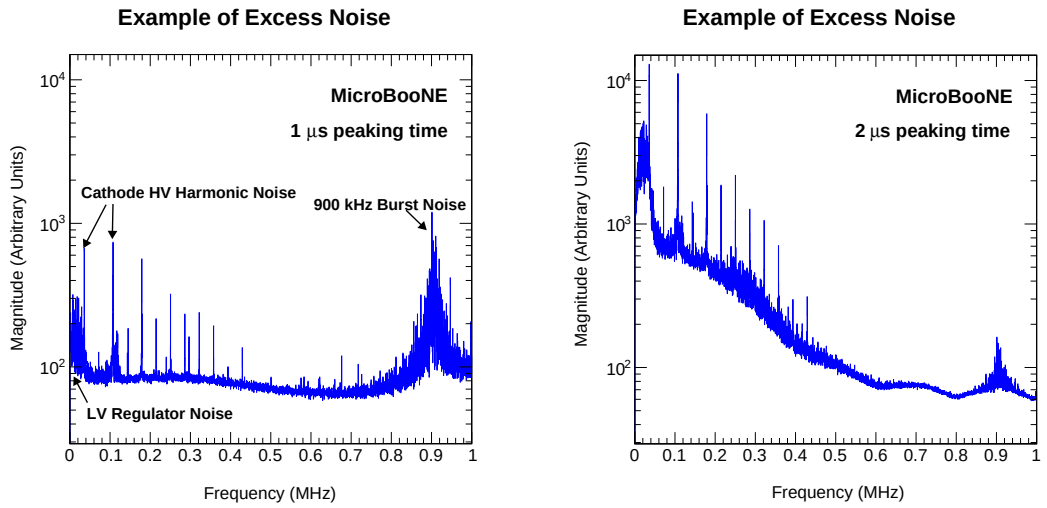

(a) (b)

Figure 10. Average noise magnitude in the frequency domain: (a) for 1 µs peaking time and 4.7 mV/fC gain settings, and (b) for 2 µs peaking time and 14 mV/fC gain settings. Three sources of excess noise are illustrated on the left panel: Low voltage (LV) regulator noise, cathode HV harmonic noise (36 kHz and 108 kHz noise), and 900 kHz burst noise.

of the HV noise is largest in the first induction plane (U) where it affects all the wires. The noise appears at a reduced level in the second induction wire plane (V), and at an even lower level in the collection wire plane (Y).

- 900 kHz burst noise: In section 5.3, the *burst* noise observed at frequencies around 900 kHz is described. This type of noise has a clear position dependence and has a burst nature. While its exact source has not yet been confirmed, evidence is pointing towards the PMT high voltage supply or the interlock system power supply.

In the following subsections, these three types of excess noise are described in detail and compared to the inherent noise in order to illustrate their impact on TPC performance. An offline filter has been developed to remove most of the excess noise. Its performance on each type of noise is described below. The filter has a negligible impact on the signal as described in the final part of this section.

5.1 Low frequency noise from voltage regulator

The most significant excess noise observed in MicroBooNE is the low frequency noise that is injected via the low voltage power input to the cold ASIC. More specifically, it is due to the voltage regulator used to provide a stable voltage for the cold ASIC. This noise source is most pronounced at low frequencies ($\lessapprox$ 30 kHz) as shown in figure 10(a). While the regulator noise is very low, it still exceeds the noise of the pMOS input transistor. The source electrode of this transistor is driven by the regulator voltage with respect to the gate electrode that is connected to a sense wire. The resulting injected noise is thus proportional to the wire capacitance. This noise is typically found to

be correlated across 192 channels on the same service board,[3] that contains the same low voltage regulator. Usually, the correlation is highest within the 48 channels covering three ASICs.

To mitigate this coherent noise, a *correction waveform* is constructed on a per sample basis and across sets of 48 contiguous channels. Initially, each sample of this waveform is set to the median of the corresponding sample tick across the 48 channels. Nominally, this correction waveform would then be subtracted from each of the 48 channels. However, certain distributions of ionization electrons, specifically those from tracks parallel to the wire planes, would otherwise be suppressed by this simple subtraction. To protect these signals, the signal height and shape of the correction waveform are examined to determine if they contain any regions above expected noise level.[4] Then, two pad regions extending 7 to 10 ticks on either side of this initial region (20 ticks towards early time for the U plane) are included. The central region of the correction waveform is then zeroed and the pad regions are linearly interpolated to zero. Finally, the resulting correction waveform is subtracted, tick-by-tick, from each of the original 48 channels.

For certain channels, the correction waveform requires additional construction before it is applied. Some of the channels on the edges of a service board recorded a larger amount of coherent noise. To reduce this, a scaling adjustment of the correction waveform is performed during subtraction for the channels on the edges of a service board. The scaling factor is calculated to be the ratio of the correlation coefficient of a single channel and the average correlation coefficient of the 48 channels.

Figure 11(d) shows an example waveform after this coherent noise removal by offline noise filtering. Section 8 describes how this coherent noise from the voltage regulators has been largely suppressed with a subsequent hardware upgrade of the service boards.

5.2 The HV power supply noise

As shown in figure 10(a), a series of narrow frequency lines appear at odd harmonics of 36 kHz which correspond to the ripple frequency of the HV power supply. The two highest peaks are near 36 kHz and 108 kHz, and other smaller harmonics are evident. The peak magnitude of this *harmonic noise* collected by channels of the first induction U plane is ≈15 ADC counts. The noise is attenuated by about a factor of three for the V plane channels due to shielding by the U plane wires and becomes negligible for the Y plane channels due to shielding by the other two wire planes.

A simple estimation for the dependence of the charge at the anode plane to tiny variations in the cathode potential, 2.5 m away, was made. For a 2.5 m wire length with a capacitance to the cathode of ≈20 fF/m,[5] the induced charge would be ≈0.05 fC/mV, resulting in ≈300 e^-/mV. The observed peak amplitude of the waveform is ≈15 ADC counts which corresponds to a charge of ≈0.5 fC. Therefore, a variation as small as ≈10 mV at the cathode can produce the observed noise. This corresponds to about five parts in 10^8 of the drift voltage.

[3] The service board mounted on the top of each signal feedthrough, provides regulated low voltage, control, and monitoring signal to the analog ASICs. It also provides pulse injection to the preamplifiers for precision calibration.

[4] The signal shape was taken into account through a deconvolution technique using a simulated signal shape for parallel tracks and fast fourier transformation. The threshold of signal height and deconvoluted signal height are all five times the corresponding noise RMS.

[5] ≈20 fF/m is the estimated value of the single wire capacitance to the cathode and is based on a planar capacitance calculation between the cathode and anode. This calculation does not include the shielding effect by the field cage, which makes the actual value smaller.

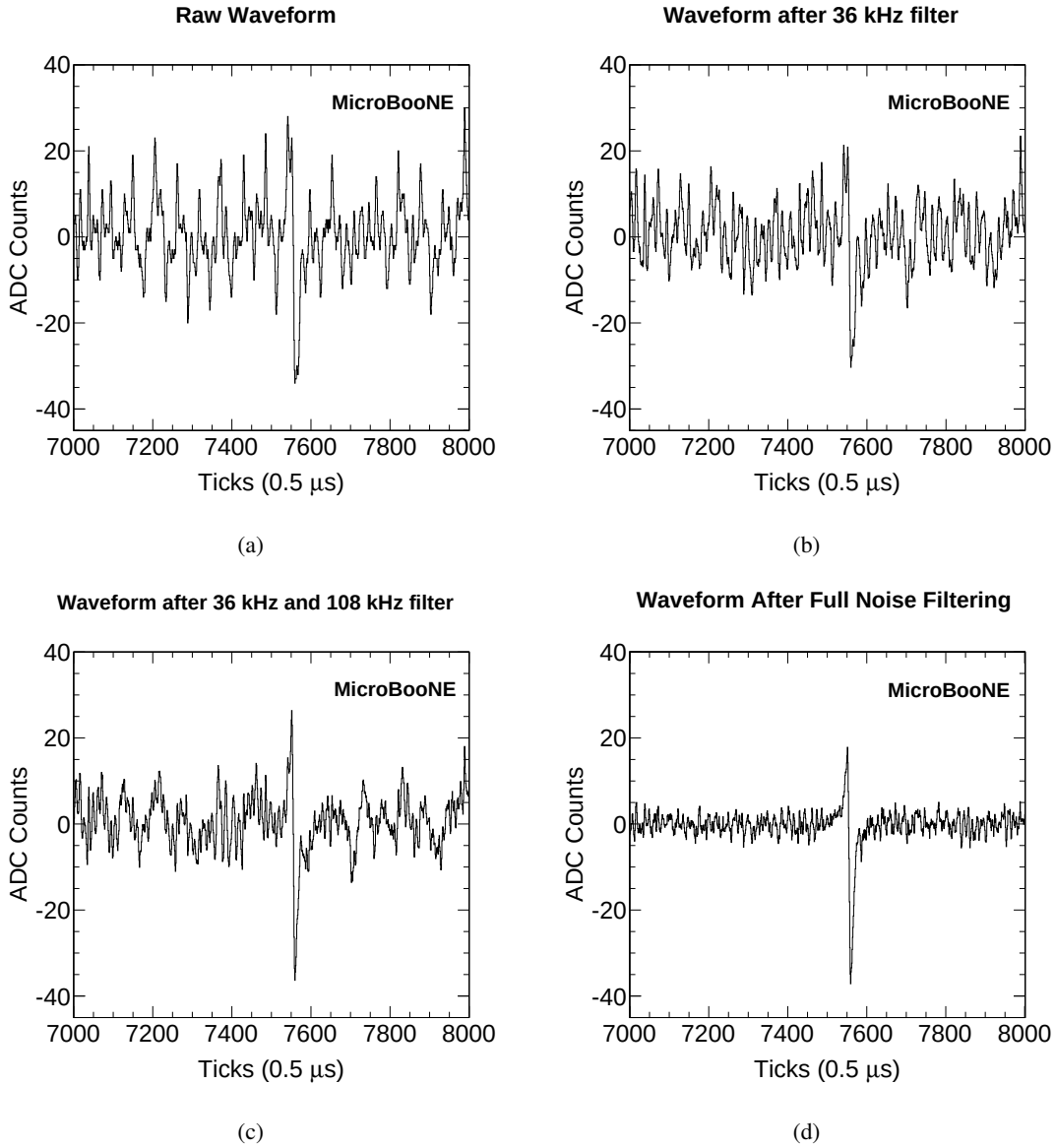

Figure 11. (a) A U plane raw waveform from data, (b) the same waveform after filtering out 36 kHz noise, (c) the same waveform after filtering out both 36 kHz and 108 kHz noise components, and (d) the waveform after the full noise filtering chain.

An offline filter directly removes this harmonic noise by masking discrete bins in the frequency domain. Figure 11(a) has no filtering applied and the bipolar signal is almost indistinguishable from noise. Figure 11(b) and 11(c) show the same waveform after filtering out the 36 kHz and 108 kHz noise, after which the characteristic bipolar induction signal can be more clearly identified. While some substantial noise remains, this is mitigated by an offline noise filter as described in section 5.3.

5.3 900 kHz **burst noise**

The least problematic excess noise is the so called "900 kHz burst noise". A waveform showing an example of this noise is shown in figure 12(a) and 12(b).

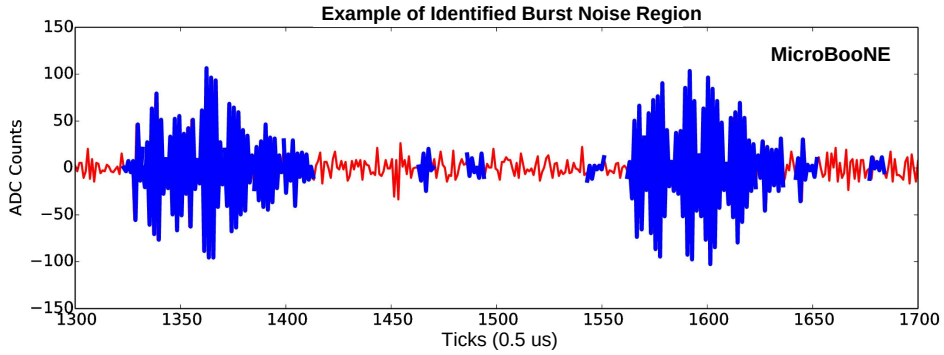

(a)

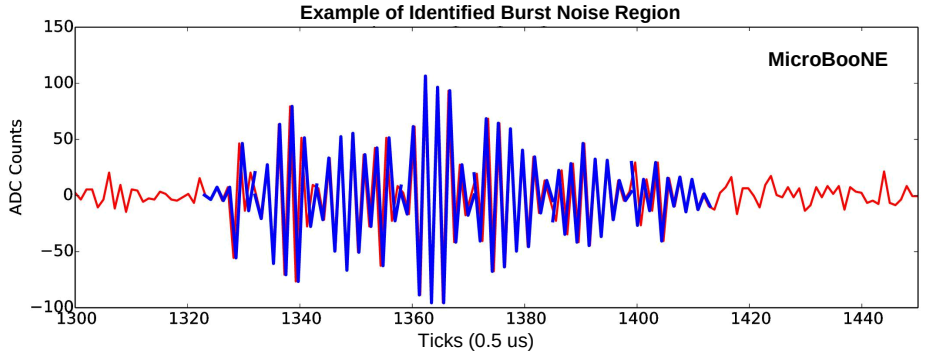

(b)

Figure 12. (a) A V plane waveform showing an example occurrence of the "900 kHz burst noise". The regions identified as exhibiting a burst of noise are highlighted in blue, and (b) zooms into the first of the two large bursts regions shown in the top panel.

The measured period of the oscillation (or ringing) seen in these bursts is 1.1 µs, as anticipated given the approximately 900 kHz peak seen in the frequency spectrum in figure 10(a). The bursts are intermittent and have amplitudes that vary over time. This noise has been observed in data from wires that are located at one corner of the detector.

No mitigation of this noise is performed as it is naturally attenuated to acceptable levels by the anti-alias filter with a 2 µs peaking time. This can be seen in a relative manner by comparing the spectra shown in figure 10(a) and 10(b). If this noise increases in the future, it can be mitigated with a simple low pass offline filter. However, in the case of the few misconfigured channels described in section 4.1, the data is taken with a 1 µs peaking time and figure 10(a) shows a prominent peak at 900 kHz. In the offline filter, the 1 µs shaping introduced by the amplifier is replaced by a 2 µs shaping filter. This results in the data from the misconfigured channels having effectively the same high frequency attenuation as the data from the nominally configured channels.

The exact origin of this burst noise has not been conclusively identified. However, the power

switching circuits related to either the PMT high voltage power supply or the interlock system power supply are currently suspected as a possible source.

5.4 Impact of noise filtering on TPC signal

In order to examine the performance of the coherent noise filter on the data, a simulated data study was conducted that overlays pulse shapes on top of recorded TPC data. The pulse shapes correspond to the average field response convolved with the readout electronics response for a given amount of ionization charge on a wire. The impact of the noise filtering process on these simulated signals is evaluated for signals produced by isolated point-like charges and for signals produced by minimum ionization tracks traveling parallel to the wire plane and perpendicular to a given wire. Signals produced by parallel tracks are expected to be most affected by the noise filter, as adjacent wires will have common signals that can be misidentified as noise by the correlated low frequency noise subtraction algorithm.

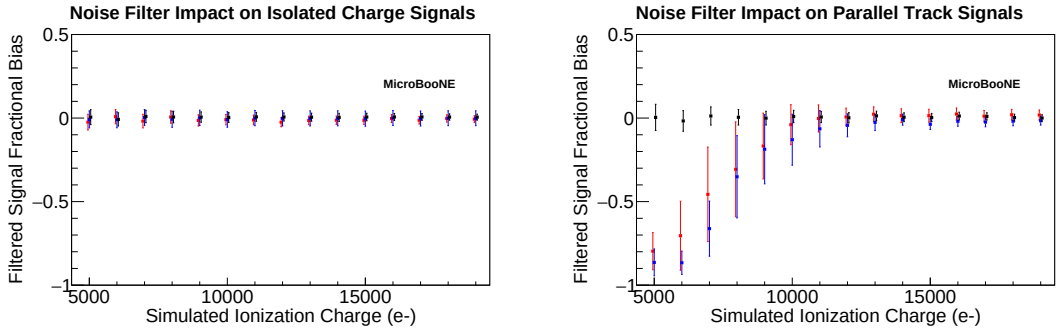

(a) (b)

Figure 13. Fractional bias of filtered signals for different amounts of simulated ionization charge in the case of (a) isolated charge; (b) charge signals produced by a track traveling parallel to the wire plane for U (red), V (blue), and Y (black) plane wires. In the case of (a) isolated ionization charge the measured bias introduced by the noise filter is consistent with zero even for very small amounts of charge. For charge signals produced by a track traveling parallel to the wire plane and perpendicular to a given wire (b) there is significant bias for small amounts of charge, but this bias becomes very small for signal sizes expected for minimum ionizing particles (≈16000 electrons).

The impact of the filtering process on ionization charge signals is evaluated by measuring the filtered signal sizes and comparing them to the expected values. The fractional bias F_{Bias} in filtered signal waveforms is defined as:

$$F_{Bias} = \frac{S_{Filter} - S_{True}}{S_{True}}, \tag{5.1}$$

where S_{Filter} is the measured filtered signal size and S_{True} is the true value used in the simulation.

The fractional bias in measured signal size as a function of simulated signal size for isolated charge signals is summarized in figure 13(a), and shows that the noise filter introduces relatively little distortion, even for very small isolated charge signals. Figure 13(b) show the measured fractional bias of filtered signals for tracks running parallel to the anode plane and perpendicular to a given wire. Small signals are distorted by the correlated noise subtraction resulting in a large fractional bias, however this effect is very small for signal sizes expected from minimum ionizing particles

(≈16000 electrons). Even for large signals, U-plane signals have a ≈2.5 % negative fractional bias due to attenuation of the long rising edge by the noise subtraction algorithm. Following the service board upgrade, the fractional bias for small filtered signals was significantly reduced.

6 Residual noise levels

An example waveform from before and after the full noise filtering procedure is shown in figures 11(a) and 11(d). The noise level for this example waveform is reduced by a factor of 3 to 5 for the induction planes and a factor of 2 to 3 for the collection plane. To give a broader picture of the effect of the noise filtering across an entire event, an example two-dimensional (2D) event display for the V plane is shown in figure 14. The noise filtering removes most of the excess noise while preserving the signal.

Figure 15 shows the residual noise in terms of the ADC RMS value after the full noise filtering is performed. There are ≈860 channels not shown here that were identified as non-functioning as described in section 4.2. The remaining channels with anomalously high ADC RMS are each examined in both the time and frequency domain. Although the observed noise frequency spectra on these channels are different from the majority of "live" channels, good induction signals can still be seen. Therefore, we keep these channels (≈84 channels in run 3455) in the data analysis.

As explained in section 3, the amount of electronics noise is expected to have a dependence on the wire length. Figure 16 shows the magnitude of the electronic noise with respect to wire length. Fitting the data with equation 3.6, gives best fit parameters of $x = 0.90$ ADC, $y = 0.79$ ADC and $z = 0.22$ ADC/m. Wire capacitance can be calculated using figure 6, which shows the variation of ENC with input capacitance, and from these fit parameters. The wire capacitance is found to be $(23 \pm 1)\,\mathrm{pF/m}$, with the two assumptions that the ENC contribution from ADC digitization is ≈150 electrons and the simulated ENC vs. input capacitance curve is solely due to the intrinsic noise. This value is within 10% of the estimations given in section 3.3.

The noise level in terms of ADC is converted to the equivalent noise charge (ENC) as follows:

$$\frac{\mathrm{ENC}}{\mathrm{ADC}} = \frac{2000\,\mathrm{mV}}{4096\,\mathrm{ADC}} \times \frac{1\,\mathrm{fC}}{14\,\mathrm{mV}} \times \frac{1}{1.2} \times \frac{6241\ e^-}{\mathrm{fC}} = 182\ \frac{e^-}{\mathrm{ADC}}. \tag{6.1}$$

The gain conversion factor given in equation 6.1 is consistent with test stand and in-situ pulser measurements. The factor of 14 mV/fC is the gain of the cold ASIC, and 1.2 is the gain of the intermediate amplifier and receiver/ADC board. As discussed in section 3.1, induction plane channels with baseline of 900 mV have ≈3% lower gain, i.e. ≈3% higher gain conversion factor than the collection plane channels with baseline of 200 mV. Therefore, the nominal ENC for the longest U plane wires is ≈400 electrons, longest V plane wires is ≈380 electrons and Y plane wires is ≈300 electrons.

Figure 17 shows the stability of the ADC RMS for same-length wires (longest wires for induction planes and all collection plane wires) over the run period from February through July, 2016. Each point in the plot is the average over ten events from a given run. From event to event, there could be fluctuation as large as ≈0.1 ADC, equivalent to 14 electrons.

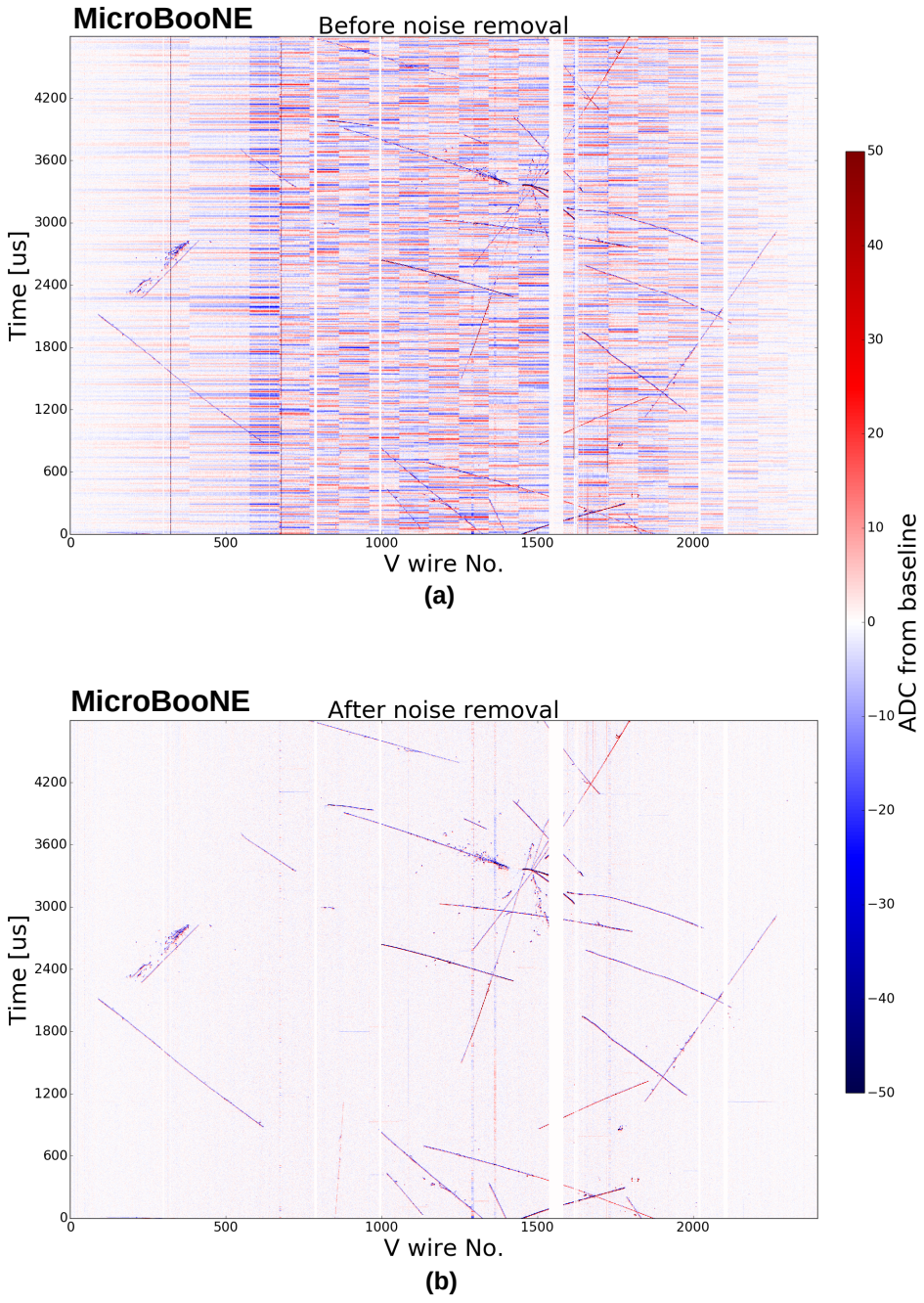

Figure 14. 2-D event display of the V plane from run 3493 event 41075 showing the raw signal (a) before and (b) after offline noise filtering. A clean event signature is recovered once all the identified noise sources are subtracted.

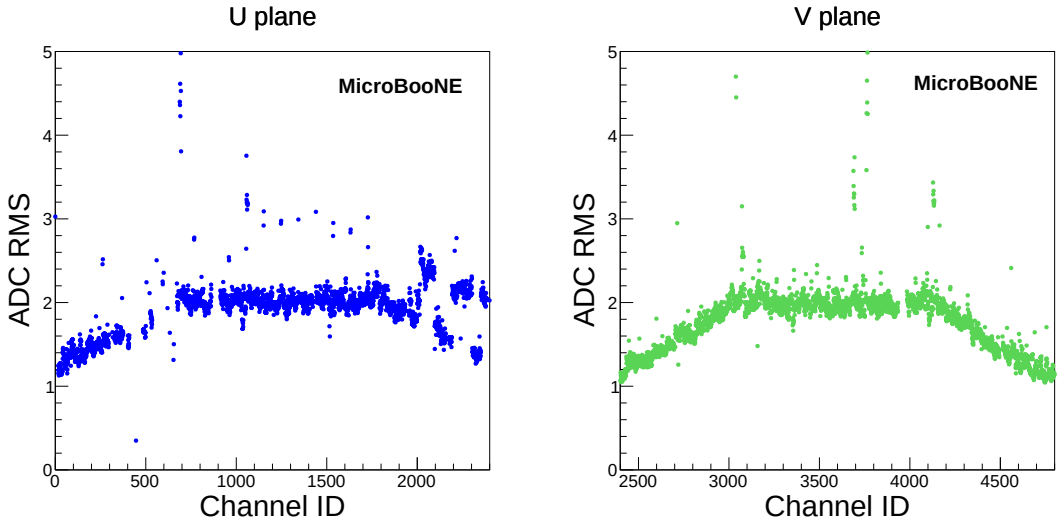

(a)

(b)

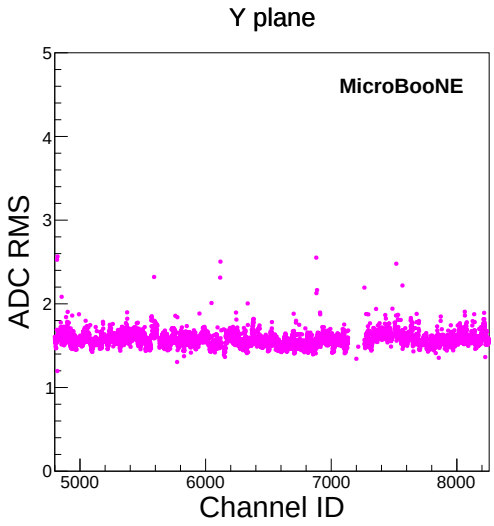

(c)

Figure 15. The residual noise level after filtering in terms of the ADC RMS value for all channels (excluding ≈860 non-functioning channels) from run 3455 event 6 is shown for (a) U, (b) V, and (c) Y planes. High RMS bands in the U plane (a) correspond to misconfigured channels as described in section 4.1. These channels are associated with larger noise as the 1 µs peaking time setting leads to ≈10% higher inherent noise than the 2 µs peaking time setting and the lowest gain setting leads to a much larger contribution of the electronics noise beyond the preamplifier.

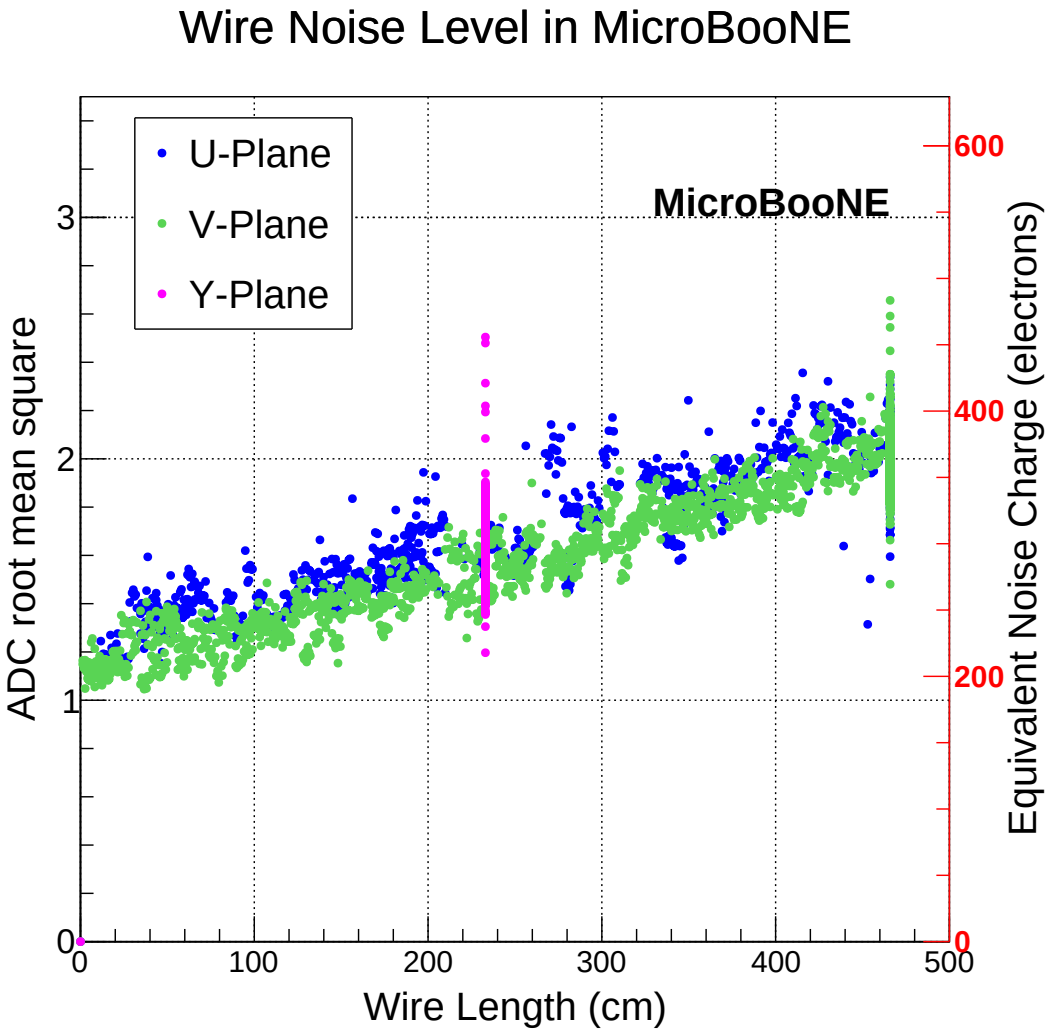

Figure 16. Noise level in terms of the ADC RMS value and ENC are plotted with respect to the wire length. The vertical band in magenta is all of the Y-plane wires which have the same length. The vertical green and blue bands at the right most end of the plot contain results from the longest (4.7 m) wires in the U and V planes which are of equal length.

7 Peak-signal to noise ratio

As charge drifts near the sense wires, the currents it induces provide a measure of its distribution in space and time. This measure is distorted by the nearby electrostatic field of the detector. In particular, the bipolar waveforms recorded on the induction plane channels are not a direct measure of the original charge distribution.

Independent of this, the amount of signal measured for a given charge distribution depends on the location and orientation of its distribution in the detector volume. Effects of diffusion and electron absorption in the LAr will reduce the measured signal as the drift distance increases. In addition, signals, particularly on the induction planes, vary substantially depending on the relative angle between a given ionization track and a sense wire.

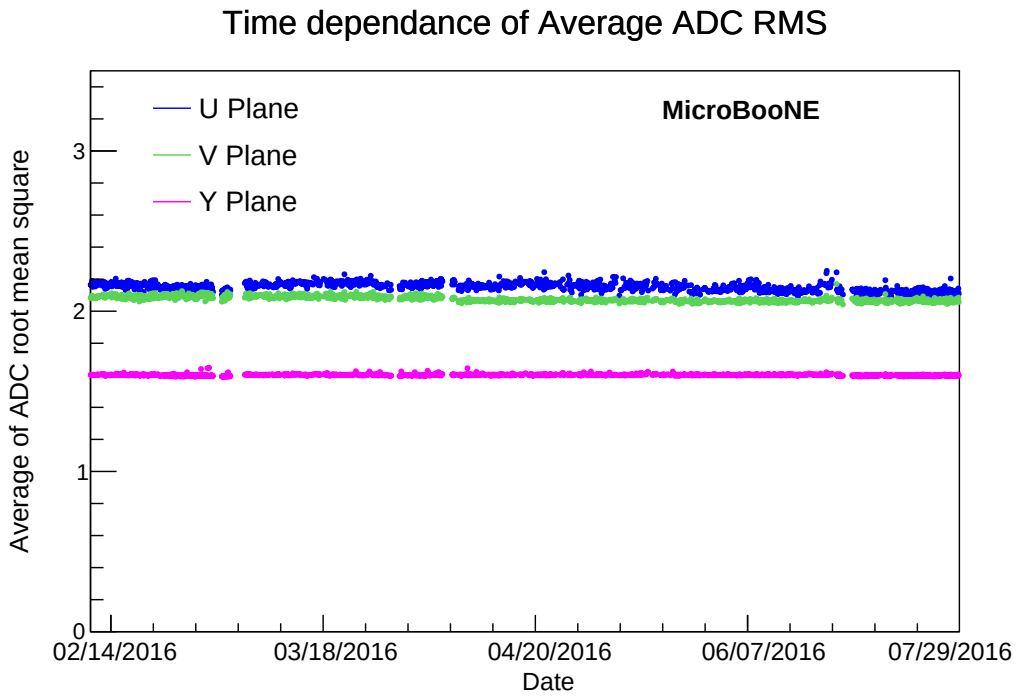

Figure 17. Average of ADC RMS for constant length U, V and Y wires as a function of time. The average is taken over ten events per run. From event to event, there could be fluctuation as large as ≈0.1 ADC or 14 electrons. This plot covers the data taking period from mid February to the end of July 2016, before the summer accelerator shutdown.

On the other hand, the excess and inherent noise are largely independent of the electrostatic field distortion and the ionization topology. As a consequence, any relative measure of signal and noise is non-trivial and likely must be constructed under various simplifying assumptions. ENC relates noise to the charge collected in a very short time (delta function). As such it can not be used to express noise relative to signals from induction wires. The requirement of a point charge of known magnitude for the signal is not possible to produce with events available in MicroBooNE data. An alternative metric that trades these limitations for others is presented here. The "peak-signal to noise ratio" (PSNR) takes for its charge distribution an ideal MIP track ("standard candle") running near and parallel to the wire planes and perpendicular to a given wire. This removes the topological variance described above. The "peak-signal" numerator is the number of electrons taken as the peak ADC sample. In the case of collection signals, this peak is a good measure of the number of nearby electrons. For induction plane signals it is only a partial, truncated measure due to the bipolar detector field response. The "noise" denominator of the ratio is simply the ADC RMS sampled outside the signal region of a given waveform.

Although the ideal standard candle is closer to the real charge distributions seen in MicroBooNE than is a point charge, statistically there are very few tracks that exactly meet this condition. To increase the sample size, tracks which otherwise come close to meeting the standard candle criteria, are allowed to pass by wires at some angle β which is not perfectly perpendicular. The resulting signal is then corrected for the geometrical factor given their reconstructed track direction.

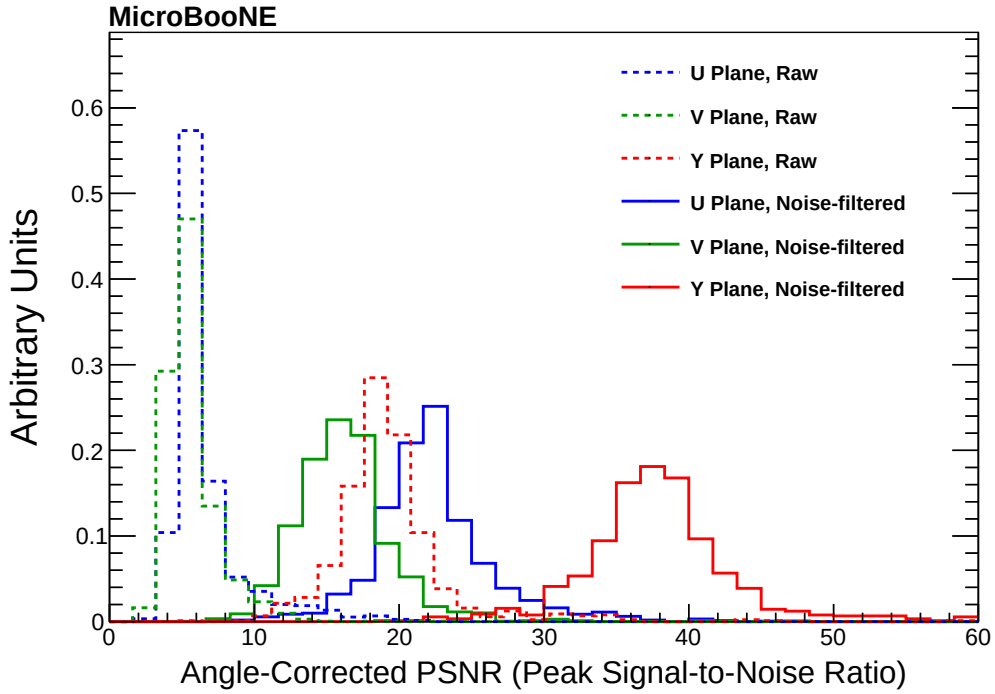

Figure 18. Angle-corrected peak-signal to noise ratio (PSNR) from a "standard candle" signal as described in the text before (dashed) and after (solid) offline noise filtering for channels in the U (blue), V (green) and Y (red) planes. Significant improvement is seen in the PSNR after the application of noise filtering due to the reduction of noise levels.

With this definition and correction in mind, the number of ionization electrons arriving at a single wire for the selected events can be estimated as

$$N_{e^-} = \frac{\frac{dE}{dx} \cdot \Delta L}{W_{\text{ionization}}} \cdot \frac{\epsilon_{\text{quenching}} \cdot \epsilon_{\text{lifetime}}}{\sin(\beta)}, \tag{7.1}$$

where the most probable energy loss $\frac{dE}{dx}$ is 1.8 MeV/cm with ≈8% fluctuation near the peak. In this case, the travel distance ΔL is the wire pitch (3 mm). $W_{\text{ionization}}$ is the average energy to generate an ionization electron in LAr and is assumed to be 23.6 eV [29]. The charge recombination factor $\epsilon_{\text{quenching}}$ [30] and the attenuation due to finite electron lifetime $\epsilon_{\text{lifetime}}$ are assumed to be 0.7 and 1.0, respectively. For a unit geometrical correction ($\sin(\beta) = 1$) the final number of ionization electrons arriving at a wire is $N_{e^-} \approx 16\,000$. Note, that the intrinsic fluctuation of energy loss per unit track length for a MIP particle inside LAr is ≈8%.

Figure 18 shows the PSNR for all three planes before and after the noise filtering. The calculation of PSNR uses a sample of t_0-tagged cosmic muon tracks,[6] near the anode plane in events collected using external triggers. Tracks traveling in a direction within 20° of parallel to the anode plane are selected and the β angular correction to their signal is made. Each track then

[6]The time (t_0) with respect to the zero time of the data acquisition system at which anode-piercing through-going cosmic ray muons enter the MicroBooNE TPC.

Table 2. Summary of the mean angle-corrected peak-signal to noise ratio (PSNR) for each plane, both before and after noise filtering using a "standard candle" signal as described in the text.

Waveform Type	U Plane PSNR	V Plane PSNR	Y Plane PSNR
Raw Data	6.6	5.7	19.5
After Noise Filtering	22.3	16.2	37.9

contributes one entry per plane to the plot using the median PSNR value associated with the track in the region of interest.

Table 2 summarizes the average PSNR values for each plane before and after noise filtering. It is clear that the PSNR for the collection plane is much higher than those of the induction plane due, in part, to their bipolar field response, as shown in figure 2. However, it is important to point out that the standard candle selection criteria tends to maximize the peak-signal of induction plane waveforms. Charge distributions from ionization tracks which point approximately normal to the wire planes will induce a signal which is prolonged in time. The bipolar response of a nearby induction plane wire will effectively cancel the middle part of the waveform and give only appreciable sample values for the portion of the waveform corresponding to the beginning and end of the ionization track. Therefore, having the lowest inherent electronic noise possible through the use of the cold front-end electronics is crucial to properly reconstruct the ionization charge information from the induction wire planes.

It is important to mention that while the PSNR metric is useful to quantify relative improvement in finding small ionization signals as a function of excess noise mitigation, it is not the most ideal metric to use to quantify improvement in the resolution of charge estimation for signals on the wires. This latter quantity is intimately tied to our capability to perform precise calorimetric measurements with ionization signals in the TPC. In order to determine how noise filtering influences charge resolution, further digital signal processing (e.g. deconvolution of electronics shaping and wire field response) is needed. Discussion of the digital signal processing chain at MicroBooNE is outside of the scope of the present work and will be presented in a future publication.

8 Hardware upgrades

As discussed previously, excess noise was identified during initial operations at MicroBooNE and mitigated via offline noise filtering methods. Subsequent to the run period covered above, and during the shutdown of the Fermilab accelerator complex over the summer of 2016, we performed two hardware upgrades an effort to further suppress the excess noise. These improvements reduced the amount of filtering required by the offline noise filter and allowed for lower zero-suppression thresholds to be used by a continuous readout system. At this time, no upgrade has been performed to mitigate the 900 kHz noise for the reasons described in section 5.3.

To reduce the the low frequency coherent noise coming from the voltage regulators, new service boards were installed that use a different voltage regulator model (ADP7159). In addition, to reduce the harmonic noise from the cathode HV power supply, a second "filter pot" (low-pass filter) was installed in the drift HV system. A comparison of the spectral noise density of the two types of voltage regulators, as well as the predicted frequency response of the one-pot and two-pot drift HV

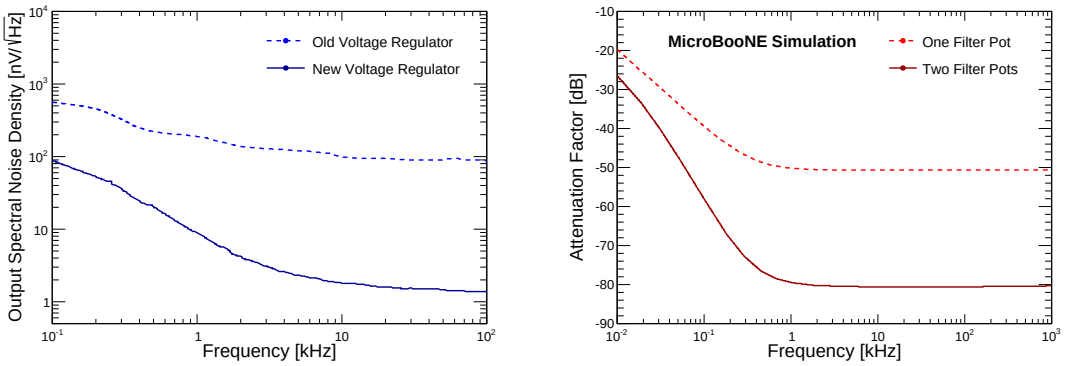

(a) (b)

Figure 19. (a) Comparison of spectral noise density for a service board with the old voltage regulator, TPS78618, and with a new low-noise voltage regulator, ADP7159. (b) Comparison of the drift HV system frequency response as predicted by a SPICE model for a single filter pot versus two identical filter pots.

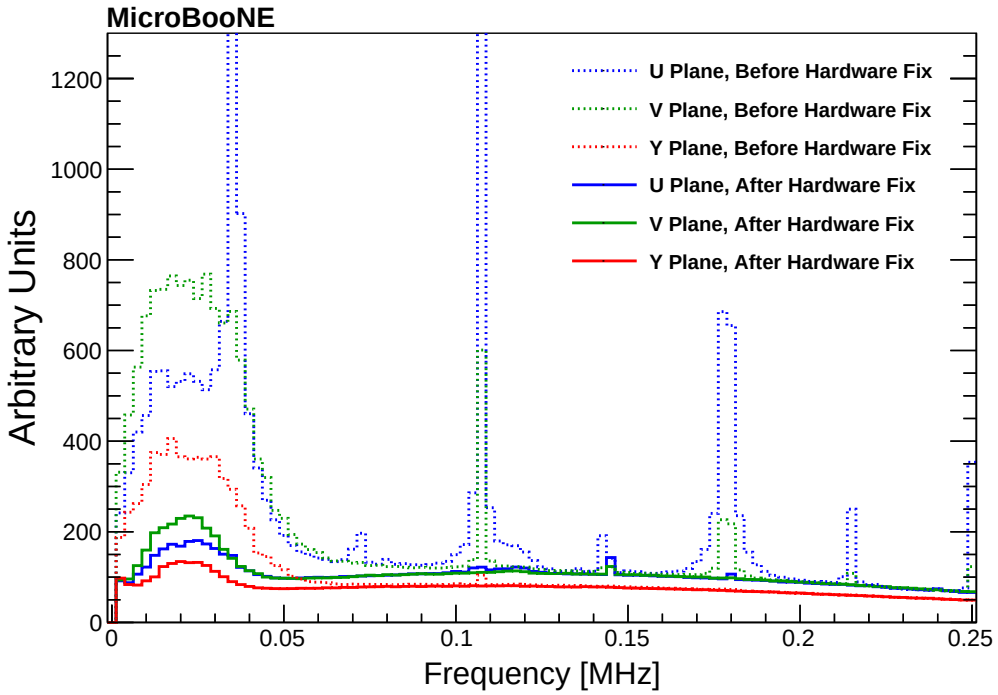

Figure 20. Comparison of the noise spectrum in the frequency domain for channels attached to the longest wires from the three planes. The data is taken from before (dashed) and after (solid) the noise mitigating hardware upgrades were performed. The plot zooms in on the frequency range of greatest interest. Note that the HV drift system was turned on (at −70 kV) at the time this data was taken, so minimum ionizing particle signals are included. The low-frequency (10 kHz to 30 kHz) noise and narrow-band (36 kHz, 108 kHz, etc.) noise types are significantly reduced by the hardware upgrades.

Table 3. Summary of ENC for the longest wires on each plane. Results for the raw data before and after the hardware upgrades are raw data without any offline noise filtering. Also shown are the results when offline noise filtering is applied to the data after hardware fixes.

Waveform Type	U Plane ENC	V Plane ENC	Y Plane ENC
Before Hardware Fix	1570	1340	640
After Hardware Fix	480	490	350
Subsequent Offline Filter	400	380	300

configurations are illustrated in figure 19(a) and 19(b). The results of the hardware upgrades are shown in figure 20, comparing the frequency content of the noise spectrum of the longest wires on each wire plane before and after the hardware noise mitigation. Both types of excess noise are dramatically reduced after the upgardes in hardware were implemented.

Table 3 summarizes the ENC associated with the pedestal regions of waveforms from the longest wires from each of the three planes, both before and after the hardware noise mitigation and also after subsequent offline noise filtering. The PSNR metrics evaluated on raw data after the hardware upgrades alone and as described above, are 18.1, 13.1 and 33.4 for the U, V, and Y planes, respectively. The hardware upgrades provided a noise suppression of about a factor of 2 for the collection plane channels, and about a factor of 3 for the induction planes.

It is important to note that there remains excess noise even after the hardware upgrades, that is largely due to the incomplete mitigation of the low frequency coherent noise from the voltage regulators. The subsequent application of the offline noise filter provides the needed additional noise suppression of 10-20%. In order to achieve the lowest possible noise levels for TPC data, offline noise filtering is still required.

9 Conclusion and outlook

In this paper, various sources of noise in the MicroBooNE TPC are described. The noise is characterized in both the frequency and time domains, as well as by wire length and channel number. The two largest sources of excess noise have been identified as originating from the TPC drift high-voltage power supply and the low-voltage regulators for the front-end ASICs. A burst of significant noise at frequencies of around 900 kHz occurs occasionally in one section of the TPC, but its exact source has yet to be identified. In addition, periodic saturation of some of the ASICs has been observed and attributed to large current induced by wire motion through the electric field caused by fluid flow.

Several offline noise filtering techniques have been developed to remove most of the excess TPC noise. Further hardware solutions have been implemented to address remaining sources of noise. The noise level (ENC) after the offline noise filtering on the data before the hardware upgrades is in general below 400 e^- for ≈90 % of MicroBooNE channels. There are 224 channels in the first induction U plane associated with an incorrect 1 µs peaking time setting that exhibit slightly higher noise. The residual noise is consistent with the cold electronics design expectations [24] and test-stand measurements and is found to be stable with time. The residual noise levels are significantly lower than those in previous experiments utilizing warm front-end electronics and

significantly improve the performance of the induction wire planes and the imaging capabilities of the TPC.

Ten percent of the channels are unusable for the physics analysis. The impact of these unusable channels depends on the reconstruction strategy.

The experience accumulated during the first year of data taking has proven to be critical in the optimization and operation of the MicroBooNE TPC and is useful in informing future LArTPC efforts. In particular, two recent hardware upgrades have significantly reduced excess noise from the cathode HV power supply and the LV regulator. The resulting noise levels after the upgrades are 3.1, 2.5, and 1.8 times better for the U, V, and Y wire planes, respectively. With the observation of ASIC saturation, a new generation of ASICs for the future Short-Baseline Neutrino (SBN) [31] program and Deep Underground Neutrino Experiment (DUNE) [32] has an added capability of setting 1 nA and 5 nA input bias currents. Spacers have also been added to support wires to reduce wire vibrations in the DUNE and SBND TPCs. These spacers are also expected to reduce the impact of potential shorts that would be present in the case of a loose wire. With the observation of misconfigured channels, the ASIC design now implements more robust electrostatic discharge protection to configuration pins. The design margin of the bandgap reference circuit was also increased in the new ASIC design to remove the "start-up" problem. As a result of this work, MicroBooNE has made critical contributions in the understanding of noise levels in LArTPCs and in further mitigating such noise sources with offline noise filtering and future design improvements.

Acknowledgments

This material is based upon work supported by the following: the U.S. Department of Energy, Office of Science, Offices of High Energy Physics and Nuclear Physics; the U.S. National Science Foundation; the Swiss National Science Foundation; the Science and Technology Facilities Council of the United Kingdom; and The Royal Society (United Kingdom). Additional support for the laser calibration system and cosmic ray tagger was provided by the Albert Einstein Center for Fundamental Physics. Fermilab is operated by Fermi Research Alliance, LLC under Contract No. DE-AC02-07CH11359 with the United States Department of Energy.

References

[1] C. Rubbia, *The Liquid-Argon Time Projection Chamber: A New Concept for Neutrino Detectors*, EP Internal Report (2015).

[2] W. Willis and V. Radeka, *Liquid-argon ionization chambers as total-absorption detectors*, *Nuclear Instruments and Methods* **120** (1974) 221.

[3] H. H. Chen, P. E. Condon, B. C. Barish and F. J. Sciulli, *A Neutrino detector sensitive to rare processes. I. A Study of neutrino electron reactions*, FERMILAB-PROPOSAL-0496.

[4] D. R. Nygren, *The Time Projection Chamber: A New 4 pi Detector for Charged Particles*, *eConf* **C740805** (1974) 58 PEP-0144.

[5] MicroBooNE collaboration, R. Acciarri et al., *Design and Construction of the MicroBooNE Detector*, *JINST* **12** (2017) , [arXiv:1612.05824].

[6] MiniBooNE collaboration, A. A. Aguilar-Arevalo et al., *The Neutrino Flux prediction at MiniBooNE*, *Phys. Rev. D.* **79** (2009) 072002, [arXiv:0806.1449].

[7] P. Adamson et al., *The NuMI Neutrino Beam*, *Nucl. Instrum. Meth.* **A806** (2016) 279–306, [arXiv:1507.06690].

[8] J. Conrad et al., *The Photomultiplier Tube Calibration System of the MicroBooNE Experiment*, *JINST* **10** (2015) , [arXiv:1502.04159].

[9] Y. Li et al., *Measurement of Longitudinal Electron Diffusion in Liquid Argon*, *Nucl. Instrum. Meth.* **A816** (2016) 160–170, [arXiv:1508.07059].

[10] W. Shockley, *Currents to Conductors Induced by a Moving Point Charge*, *Journal of Applied Physics* **9** (1938) 635.

[11] S. Ramo, *Currents Induced by Electron Motion*, *Proceedings of the ORE* **27** (1939) 584.

[12] O. Bunemann, T. Cranshaw and J. Harvey, *Design of Grid Ionization Chambers*, *Can. J. Research* **27A** (1949) .

[13] MicroBooNE Technical Design Report, http://www-microboone.fnal.gov/publications/TDRCD3.pdf.

[14] R. Veenhof, *GARFIELD, recent developments*, *Nucl. Instrum. Meth.* **A419** (1998) 726–730.

[15] V. Radeka et al., *Cold electronics for 'Giant' Liquid Argon Time Projection Chambers*, *J. Phys. Conf. Ser.* **308** (2011) 012021.

[16] MicroBooNE collaboration, R. Acciarri et al., *Construction and Assembly of the Wire Planes for the MicroBooNE Time Projection Chamber*, *JINST* **12** (2017) , [arXiv:1609.06169].

[17] http://analog.com/media/en/technical-documentation/data-sheets/AD9222.pdf.

[18] G. Gielen, *Analog building blocks for signal processing*, *Leuven: KULeuven-ESAT-MICAS* (2006) .

[19] H. Nyquist, *Thermal Agitation of Electric Charge in Conductors*, *Phys. Rev.* **32** (Jul, 1928) 110–113.

[20] T. O'Haver, *Intro to Signal Processing - Deconvolution*, University of Maryland at College Park.

[21] V. Radeka, *Signal Processing for Particle Detectors*, Springer Handbook I21B1 Chapter 3.6.

[22] A. Pullia and A. Riboldi, *Time-Domain Simulation of Electronic Noises*, *IEEE Transactions on Nuclear Science* **51** (2004) 1817–1823.

[23] V. Radeka, *Low Noise Techniques in Detectors*, *Ann. Rev. Nucl. Part. Sci.* **38** (1988) 217–277.

[24] G. De Geronimo et al., *Front-end ASIC for a Liquid Argon TPC*, *IEEE Trans. Nucl. Sci.* **58** (2011) 1376–1385.

[25] G. A. Erskine, *Electrostatic problems in multiwire proportional chambers*, *Nucl. Instrum. Meth.* **105** (1972) 565–572.

[26] P. Van Esch, *Capacity formulas in MWPC: Some critical reflections*, *JINST* **1** (2006) P12001.

[27] MicroBooNE collaboration, H. Chen et al., *A Proposal for a New Experiment Using the Booster and NuMI Neutrino Beamlines: MicroBooNE*, FERMILAB-PROPOSAL-0974.

[28] B. C. et al., *Design and Operation of A Setup with A Camera and Adjustable Mirror to Inspect the Sense-Wire Planes of the Time Projection Chamber Inside the MicroBooNE Cryostat*, *JINST* **10** (2015) , [arXiv:1507.02508].

[29] http://lar.bnl.gov/properties/.

[30] ArgoNeuT collaboration, R. Acciarri et al., *A study of electron recombination using highly ionizing particles in the ArgoNeuT Liquid Argon TPC*, *JINST* **8** (2013) P08005, [arXiv:1306.1712].

[31] LAr1-ND, ICARUS-WA104, MicroBooNE collaboration, M. Antonello et al., *A Proposal for a Three Detector Short-Baseline Neutrino Oscillation Program in the Fermilab Booster Neutrino Beam*, arXiv:1503.01520.

[32] DUNE collaboration, R. Acciarri et al., *Long-Baseline Neutrino Facility (LBNF) and Deep Underground Neutrino Experiment (DUNE) Conceptual Design Report Volume 1: The LBNF and DUNE Projects*, arXiv:1601.05471.